

Nonlinear and buoyancy pressure correlations in stably stratified turbulence

Young Ro Yi^{1,2} , Jeffrey Russell Koseff¹ and Elie Bou-Zeid³

¹Bob and Norma Street Environmental Fluid Mechanics Laboratory, Department of Civil and Environmental Engineering, Stanford University, Stanford, CA 94305, USA

²High Meadows Environmental Institute, Princeton University, Princeton, NJ 08544, USA

³Department of Civil and Environmental Engineering, Princeton University, Princeton, NJ 08544, USA

Corresponding author: Young Ro Yi, yryi@princeton.edu

(Received 21 August 2024; revised 8 August 2025; accepted 16 August 2025)

We analyse direct numerical simulations of homogeneous, forced, stably stratified turbulence to study how the pressure–strain and pressure scrambling terms are modified as stability is increased from near neutral to strongly stratified conditions. We decompose the pressure into nonlinear and buoyancy components, and find that the buoyancy part of the pressure–strain correlation changes sign to promote large-scale anisotropy at strong stability, unlike the nonlinear component, which always promotes large-scale isotropy. The buoyancy component of the pressure scrambling term is positive semidefinite and increases monotonically with stability. As its magnitude becomes greater than the nonlinear component (which is negative), the overall scrambling term generates buoyancy flux at very strong stability. We apply quadrant analysis (in the pressure–gradient space) to these correlations to study how contributions from the four quadrants change with stability. Furthermore, we derive exact relationships for the volume-averaged buoyancy components of these correlations which reveal (i) the buoyancy component of the pressure–strain correlation involves a weighted sum of the vertical buoyancy flux cospectrum, so counter-gradient buoyancy fluxes contribute to enhanced anisotropy by transferring vertical kinetic energy into horizontal kinetic energy; (ii) the buoyancy component of the pressure scrambling term involves a weighted sum of the potential energy spectrum; (iii) the weighting factor accentuates contributions from layered motions, which are a prominent feature of strongly stratified flows. These expressions apply generally to all homogeneous stratified flows independent of forcing and across all stability conditions, explaining why these effects have been observed for both forced and sheared stably stratified turbulence simulations.

Key words: stratified flows, turbulent mixing, stratified turbulence

1. Introduction

Density stratification is a prominent feature of both atmospheric and oceanic flows, affecting the vertical exchange of quantities such as mass, momentum and heat. Therefore, developing a more robust physical understanding of stratified turbulence is of benefit for a wide range of applications in Earth science. For wind energy, stratification influences the upstream wind profile and the downstream wake characteristics, affecting both the individual and collective performance of turbines (Stevens & Meneveau 2017; Porté-Agel *et al.* 2020). In high-latitude environments such as the Arctic, stable atmospheric boundary layers form over ice, reducing the vertical exchange of heat, in particular, and affecting warming projections (Bintanja, van der Linden & Hazeleger 2012; Audouin *et al.* 2021; Allouche *et al.* 2022; Fogarty & Bou-Zeid 2023). In the surface ocean, submesoscale flows (with horizontal scales between 0.2 and 20 km) interact with and modify the vertical stratification (Taylor & Thompson 2023), influencing the exchange of biogeochemical tracers such as carbon and nutrients across the surface mixed layer and impacting ocean ecosystems (Lévy *et al.* 2018). Finally, due to the wide range of spatial and temporal scales of oceanic flows (Wunsch & Ferrari 2004), global ocean simulations rely on down-gradient closures to represent subgrid-scale (unresolved) fluxes of momentum, scalars like heat and salt (e.g. Adcroft *et al.* 2019; Fox-Kemper *et al.* 2019), and biogeochemical tracers (e.g. Henson *et al.* 2022; Lévy *et al.* 2024). The resulting vertical tracer and density distributions, as well as meridional transport, are sensitive to the choice of subgrid-scale models and how well they capture the impact of stratification (e.g. Bryan 1987; Gnanadesikan 1999; Jayne 2009; de Lavergne *et al.* 2016; Mashayek *et al.* 2017; Cimoli *et al.* 2019; Lévy *et al.* 2001; Resplandy, Lévy & McGillicuddy 2019).

This work examines the impact of density stratification through the lens of this final application, focusing on modelling of subgrid-scale fluxes in global ocean models (though the fundamental physics are also applicable to atmospheric flows), particularly the vertical buoyancy fluxes that are often estimated using an eddy diffusivity model following Osborn (1980). We provide a non-dimensional form from Salehipour & Peltier (2015),

$$\frac{D_T}{D} = \left(\frac{Ri_f}{1 - Ri_f} \right) \frac{\epsilon_k}{DN^2} = \Gamma \left(\frac{\epsilon_k}{\nu N^2} \right) \left(\frac{\nu}{D} \right) = \Gamma Re_b Pr, \quad (1.1)$$

where D_T and D are the turbulent and molecular diffusivities of the stratifying scalar; Ri_f is the mixing efficiency (also referred to as the flux Richardson number), which typically represents the mean fraction of the energy input that is used to irreversibly mix the stratifying scalar field; $\Gamma = Ri_f/(1 - Ri_f)$ is the mixing coefficient (also referred to as the flux coefficient); ϵ_k is the dissipation rate of turbulent kinetic energy; ν is the kinematic viscosity of the fluid; $N^2 = -(g/\rho_0)d_z\bar{\rho}$ is the vertical background stratification; $Re_b = \epsilon_k/(\nu N^2)$ is the buoyancy Reynolds number, which quantifies the intensity of a stratified turbulent flow; and $Pr = \nu/D$ is the molecular Prandtl number. Several definitions of the flux Richardson number (and relatedly Γ) exist in the literature. Two commonly used forms are the reversible and irreversible definitions ($Ri_{f,r} = B/P_k$ and $Ri_f = \epsilon_p/(\epsilon_k + \epsilon_p)$, respectively; cf. Venayagamoorthy & Koseff 2016), where B is the vertical buoyancy flux (equivalent to the rate of conversion of turbulent kinetic energy into turbulent potential energy associated with the density perturbations when there is no direct forcing of potential energy), P_k the rate of shear production of turbulent kinetic energy and ϵ_p the dissipation rate of turbulent potential energy. When statistical stationarity and homogeneity hold, the two definitions become equivalent because $B = \epsilon_p$ and $P_k = \epsilon_k + \epsilon_p$, but there are key differences between the two when the turbulent flow is unsteady and/or inhomogeneous (cf. Ivey & Imberger 1991; Chamecki, Dias & Freire

2018; Freire *et al.* 2019). Hereafter, we will primarily refer to and use the irreversible definition.

Equation (1.1) can be useful for estimating the eddy diffusivity for global ocean models since the molecular Prandtl number and diffusivity are known and there exists Re_b estimates from field measurements of ϵ_k and N^2 via microstructure profilers and conductivity-temperature-depth (CTD) casts. The only missing part, then, is relating Γ to easily accessible or measurable quantities (see the reviews by Ivey, Winters & Koseff 2008; Gregg *et al.* 2018; Caulfield 2020, 2021). Here, we provide brief overviews of two specific approaches. The first approach involves relating Γ to Re_b . For example, Monismith, Koseff & White (2018) analysed a large collection of laboratory experiments, field measurements and numerical simulations of different types of stably stratified turbulent flows, and showed that many of the datasets exhibited a constant value of Ri_f , and thus Γ , for $Re_b < 100$ and a scaling $Ri_f \sim Re_b^{-1/2}$ for $Re_b > 100$, though some datasets exhibited this transition at values of Re_b much larger than 100. While Re_b attempts to quantify the turbulence intensity in stably stratified conditions, there is an ambiguity associated with the parameter because the same value of Re_b can be achieved in both weakly and strongly stratified conditions with appropriate differences in turbulence levels between the two states. For example, there should be negligible mixing of the background buoyancy field in near neutral conditions compared with strongly stratified conditions even though the two flows might be characterised by the same value of Re_b . Nevertheless, this approach is easier to implement in global ocean models given that parametrisations for ϵ_k already exist (e.g. St. Laurent, Simmons & Jayne 2002; Polzin 2009) and, therefore, applying (1.1) only requires choosing a particular form of $\Gamma = f(Re_b)$ (de Lavergne *et al.* 2016).

An alternative approach involves relating Γ and the turbulent Froude number ($Fr_k = \epsilon_k / (Nk)$), where k is the turbulent kinetic energy (TKE). By considering that the buoyancy Reynolds number can be rewritten as $Re_b = Re_L Fr_k^2$, where $Re_L = k^2 / (\nu \epsilon_k)$ is the large-eddy Reynolds number, Maffioli, Brethouwer & Lindborg (2016) analysed simulations of homogeneous, forced, stably stratified turbulence and showed that Γ varies strongly with Fr_k . However, for weak stability, Γ also decreased with Reynolds number (the Taylor Reynolds number Re_λ in particular; see their figures 1 and 3). Relatedly, Bragg & de Bruyn Kops (2024a) analysed simulations of homogeneous, vortically forced, stably stratified turbulence. While they confirmed the strong relationship between Γ and Fr_k , they observed that Γ increases with Reynolds number for weak stability (see their figure 4), in contrast to the findings of Maffioli *et al.* (2016). This clearly demonstrates an interplay between how the turbulence is forced (only horizontal forcing and no vertical forcing in Bragg & de Bruyn Kops (2024a) versus horizontal and vertical forcing in Maffioli *et al.* (2016) for most of their simulations) and the relationship between Γ and the Reynolds number. Also, Portwood, de Bruyn Kops & Caulfield (2019) analysed simulations of homogeneous, sheared, stably stratified turbulence and observed that Γ was approximately constant as Re_b was varied across approximately two orders of magnitude due to limited variations in the Froude number (see their figure 3a and table 1). Other works have also demonstrated a strong relationship between Γ and Fr_k (e.g. Garanaik & Venayagamoorthy 2019; Howland, Taylor & Caulfield 2020; Issaev *et al.* 2022; Tu *et al.* 2022; Yi & Koseff 2022a; Nguyen-Dang *et al.* 2023), but Γ is known to depend also on other physical effects such as mean shear (e.g. Mater & Venayagamoorthy 2014a,b; Yi & Koseff 2022b), the presence of a buoyancy-driven component to the forcing (e.g. Howland *et al.* 2020; Lewin & Caulfield 2022) and the Prandtl number (e.g. Salehipour, Peltier & Mashayek 2015; Rahmani, Seymour & Lawrence 2016; Legaspi & Waite 2020; Riley, Couchman & de Bruyn Kops 2023; Petropoulos *et al.* 2024; Bragg & de Bruyn Kops 2024b).

To probe this interplay between forcing and the turbulence-mixing relation, here, we seek to build on the findings of Yi & Koseff (2022a) and Yi & Koseff (2023), where four different types of homogeneous, forced, stably stratified turbulence were simulated. The Reynolds stress and buoyancy flux budgets were analysed as a function of increasing stability from near neutral to strongly stable conditions. Despite the differences in forcing (unsheared versus three different orientations of shear forcing relative to a background vertical stratification), all four datasets exhibited strong relationships among the pressure–strain redistribution term (source/sink in the vertical velocity variance budget), the pressure scrambling term (pressure–scalar gradient correlation; source/sink in the vertical buoyancy flux budget) and the mixing coefficient Γ . This general behaviour likely stems from the fact that, in all four of these datasets, stable stratification promotes large-scale anisotropy by damping vertical motions (the largest ones first), and that pressure–strain correlations act to redistribute the more energetic components of the TKE to the less energetic ones (recall that TKE comprises the diagonal Reynolds stresses). The physical picture associated with this description of the pressure–strain correlations is at the heart of Rotta’s return-to-isotropy model, where Reynolds stress anisotropy decays exponentially in time in the absence of forcing (Rotta 1951). For passive scalar fluxes, the pressure scrambling terms usually act as major sinks, decorrelating the velocity and scalar fields (Hao & Górlé 2020). For vertical buoyancy fluxes, however, the pressure scrambling terms were shown to change sign as stability was increased, becoming a major source of vertical buoyancy flux at very strong stability (Yi & Koseff 2022a, 2023).

To better understand the role of pressure fluctuations in stratified turbulence, we study the pressure–strain correlations and pressure scrambling terms using the DNS dataset of homogeneous, forced, stably stratified turbulence that was presented by Yi & Koseff (2022a). Our goals are threefold: (i) study how the nonlinear and buoyancy components of the pressure correlations change with increasing stability; (ii) develop and provide physical intuition and interpretation for the nonlinear and buoyancy pressure correlations; and (iii) connect these changes to irreversible mixing of density quantified by the variation of the mixing coefficient Γ as a function of increasing stability as characterised by Fr_k .

Our paper is organised as follows. In § 2, we explore the relationship between Ri_f (and relatedly Γ) and the various governing parameters of stably stratified turbulence by considering the volume-averaged budgets of the components of TKE and TPE, highlighting the key role that pressure–strain redistribution plays in setting the mixing efficiency. In § 3, we briefly describe the dataset of homogeneous, forced, stably stratified turbulence and summarise the key results from Yi & Koseff (2022a), which motivate the subsequent derivations and analyses in this work. In § 4, we decompose the pressure fluctuations based on the pressure Poisson equation to study the nonlinear and buoyancy components of pressure–strain and pressure scrambling terms as a function of increasing stability. We provide physical explanations for the two sets of positive and negative pressure fluctuations based on their respective Poisson equations, and also derive analytical expressions for the buoyancy components of the pressure–strain and pressure scrambling terms, which aid with interpreting their empirically observed behaviour from DNS with increasing stability. We conclude our paper in § 5.

2. Relationship between pressure–strain redistribution and mixing efficiency

One way to reframe the question of how Γ varies with Re_b and Fr_k is to ask how Γ depends on the ranges of isotropic versus anisotropic scales of stably stratified turbulence. To do so, we introduce three different length scales: (i) $\eta_k = (v^3/\epsilon_k)^{1/4}$ (Kolmogorov length scale, an estimate of the size of the smallest turbulent eddies); (ii) $l_O = (\epsilon_k/N^3)^{1/2}$ (Ozmidov

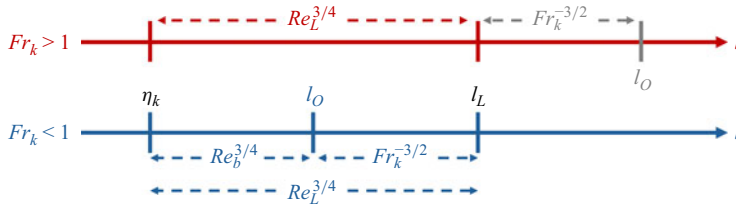


Figure 1. An illustration of the range of turbulent scales in stably stratified turbulence. Stratification effects are weak for $Fr_k > 1$ (red), and the range of active turbulent scales are better characterised by Re_L . Scales between l_L and l_O are not relevant (grey) since the size of the most energetic eddies are better described by l_L . Stratification effects are significant for $Fr_k < 1$ (blue). Here, the range of active isotropic scales are better characterised by Re_b , and the range of active anisotropic scales are characterised by Fr_k . The entire range of scales (both isotropic and anisotropic) is represented by Re_L .

length scale, below which the effects of buoyancy are negligible; Dalaudier & Sidi 1990; Katul *et al.* 2014); and (iii) $l_L = k^{3/2}/\epsilon_k$ (large-eddy or integral length scale). For sheared stably stratified turbulence, one has to also consider $l_C = (\epsilon_k/S^3)^{1/2}$ (Corrsin length scale, below which the effects of mean shear are negligible), which can be accounted for either through a non-dimensional shear parameter $S_* = Sk/\epsilon_k$ or the gradient Richardson number $Ri_g = N^2/S^2$. For stably stratified turbulence with realistic molecular diffusivities of heat and salt in the ocean ($Pr = \nu/D_{heat} \approx 7$ and $Sc = \nu/D_{salt} \approx 700$), one would have to consider $l_B = (\nu D^2/\epsilon_k)^{1/4} = \eta_k Pr^{-1/2}$ (Batchelor length scale, an estimate of the scale of the smallest scalar variability) as well. Here, we focus just on the simplest case where the forcing does not directly impose a mean shear and when the molecular diffusivities of momentum and the stratifying scalar are equal ($Pr = 1$, implying that $l_B = \eta_k$). Under these assumptions, we can form length-scale ratios and relate them to Re_L , Re_b and Fr_k , where $Re_L = k^2/(\nu\epsilon_k) = (l_L/\eta_k)^{4/3}$, $Re_b = \epsilon_k/(\nu N^2) = (l_O/\eta_k)^{4/3}$ and $Fr_k = \epsilon_k/(Nk) = (l_L/l_O)^{-2/3}$ (note that any of these ratios can be written as a function of the other two). For $Fr_k > 1$, the Ozmidov scale is larger than the large-eddy length scale and, therefore, buoyancy has negligible impact on the dynamics of the active turbulent scales. Therefore, in that regime, Re_L better represents the active range of turbulence scales than Re_b (see the top half of figure 1 and also Maffioli *et al.* 2016). For $Fr_k < 1$, the Ozmidov scale is smaller than the large-eddy length scale; therefore, Re_b represents the active range of isotropic scales (assuming there are no other drivers of anisotropy except buoyancy) that are insignificantly influenced by stratification, while Fr_k represents the active range of anisotropic scales, strongly influenced by stratification (see the bottom half of figure 1). For a similar schematic that incorporates the effect of mean shear, see figure 2 of Mater & Venayagamoorthy (2014b).

To connect the ideas of the range of isotropic and anisotropic scales to the mixing efficiency and the turbulent diffusivity in (1.1), we consider a generalised set of volume-averaged budgets for the three components of TKE (k_u , k_v and k_w) and TPE (k_p) for homogeneous stably stratified turbulence,

$$d_t k_u = P_u + R_u - \epsilon_u, \quad (2.1)$$

$$d_t k_v = P_v + R_v - \epsilon_v, \quad (2.2)$$

$$d_t k_w = P_w + R_w - B - \epsilon_w, \quad (2.3)$$

$$d_t k_p = P_p + B - \epsilon_p. \quad (2.4)$$

In (2.1)–(2.4), the subscripts u , v and w indicate terms associated with the x , y and z directions; P_u , P_v and P_w represent the mechanical production of k_u , k_v and k_w by forcing; P_p represents the buoyant production or loss of k_p by processes such as radiative

heating/cooling (e.g. Williamson *et al.* 2015) or the propagation of internal gravity waves (e.g. Howland *et al.* 2020); R_u , R_v and R_w represent redistribution by pressure–strain correlations; B is the vertical buoyancy flux representing the exchanges between TKE and TPE; and ϵ_u , ϵ_v , ϵ_w and ϵ_p represent the dissipation of k_u , k_v , k_w and k_p . Following similar steps as Bou-Zeid *et al.* (2018), we seek an alternative expression for the mixing efficiency. We assume statistical stationarity, introduce a dissipation anisotropy factor $c_3 = \epsilon_w/\epsilon_k$ and re-express the dissipation term in (2.3) as $\epsilon_w = c_3\epsilon_k$. Then, we use (2.4) to re-express the vertical buoyancy flux as $B = \epsilon_p - P_p$, and use the total energy balance between production and dissipation ($P_k + P_p = \epsilon_k + \epsilon_p$) to re-express the TKE dissipation term. Finally, we divide by the total mechanical production $P_k = P_u + P_v + P_w$ and isolate the irreversible mixing efficiency $Ri_f = \epsilon_p/P_k$ to arrive at

$$Ri_f = \frac{1}{1 - c_3} \left(\frac{P_w}{P_k} + \frac{R_w}{P_k} - c_3 \right) + \frac{P_p}{P_k}, \quad (2.5)$$

where P_w/P_k represents the fraction of the mechanical production that occurs in the z -direction; R_w/P_k represents the relative importance of redistribution by pressure–strain in the z -direction compared with mechanical production; c_3 is a measure of small-scale anisotropy ($c_3 = 1/3$ when the finest dissipative scales are isotropic); and P_p/P_k represents the relative importance of buoyancy production or destruction of k_p through some external forcing to mechanical production.

If buoyancy generation is positive ($P_p/P_k > 0$) and the other terms change insignificantly, one obtains larger values of Ri_f relative to a baseline scenario where $P_p/P_k = 0$. However, when $P_p/P_k \gg 1$, resulting in $k_p > k_w$, the vertical buoyancy flux can reverse signs leading to $B < 0$ as in buoyancy-driven systems, complicating the prediction of Ri_f relative to a baseline scenario of $P_p/P_k = 0$. If buoyancy generation is negative ($P_p/P_k < 0$) and the other terms change insignificantly, this effectively promotes greater stability and would lead to smaller values of Ri_f relative to a baseline scenario where $P_p/P_k = 0$.

Next, we set $P_p/P_k = 0$ in (2.5), which corresponds to the absence of large-scale buoyancy generation or destruction, for this allows us to connect more directly to the majority of studies in the stably stratified turbulence literature. This leads to

$$Ri_f = \frac{1}{1 - c_3} \left(\frac{P_w}{P_k} + \frac{R_w}{P_k} - c_3 \right), \quad (2.6)$$

which we now use to explore how Ri_f can vary for different sets of homogeneous, forced, stably stratified turbulence simulations. The first class of flows involves $P_w/P_k \neq 0$, but $0 < P_w/P_k < 1$, which corresponds to flows where there is non-zero generation of k_w by forcing but not all of the mechanical production goes to generating w . This includes the physical-space, linear velocity forcing used by Yi & Koseff (2022a) as well as the spectral-space, low-wavenumber forcing used by Maffioli *et al.* (2016). As stability is increased (e.g. decreasing Fr_k) while keeping c_3 fixed (maintaining the isotropic range of scales; keeping Re fixed with $Re = Re_L$ for $Fr_k > 1$ and $Re = Re_b$ for $Fr_k \leq 1$), P_w/P_k is expected to decrease since a larger energy input is required in the horizontal directions to maintain three-dimensional (3-D) turbulence. Furthermore, the vertical component of TKE becomes smaller than the horizontal components, implying that, on average, pressure–strain redistribution would take more energy from k_u and k_v to generate k_w ($R_w/P_k > 0$).

The second class of flows involves $P_w/P_k = 0$. This includes a wide range of forcing schemes that only inject energy to the horizontal velocity fields (e.g. random forcing in spectral space, Lindborg 2006; vortical forcing in spectral space, Waite & Bartello 2004)

as well as scenarios that involve wall-bounded flows (specifically away from boundaries where transport effects are weak) or mean shear such that there is only production of k_u and/or k_v (e.g. Shih *et al.* 2005; Basak & Sarkar 2006; Shah & Bou-Zeid 2014). Because vertical motions are not forced, these simulations involve large-scale anisotropy even in the limit of neutral stratification. Therefore, $R_w/P_k > 0$ is required for three-dimensional turbulence. As stability increases (keeping the small-scale anisotropy factor c_3 fixed), changes in Ri_f could only arise from changes in R_w/P_k , which represents the fraction of the mechanical production that gets used to generate vertical motions via pressure–strain redistribution.

The third class of flows involves $P_w/P_k = 1$, where all of the mechanical production occurs in the vertical velocity field. This is the limiting case of physical scenarios that might involve vertical motions such as obliquely propagating internal gravity waves and the interaction of buoyant jets and plumes with a background stratification (e.g. Gayen & Sarkar 2011; Williamson, Armfield & Lin 2011; Onuki, Joubaud & Dauxois 2021; Lewin & Caulfield 2022). Since mechanical production only occurs in the vertical direction, $R_w/P_k < 0$ is required for three-dimensional turbulence. Therefore, with increasing stability (keeping the small-scale anisotropy factor c_3 fixed), the mixing efficiency Ri_f is determined by how effectively energy is redistributed from k_w into k_u and k_v .

Lastly, in all of these scenarios, simultaneous variations of the range of isotropic and anisotropic scales (i.e. Re_L , Re_b and Fr_k varying simultaneously) would involve simultaneous variations of P_w/P_k , R_w/P_k and c_3 . Because we have used the irreversible definition of the mixing efficiency in (2.6), we can explore how Ri_f depends on P_w/P_k , R_w/P_k and c_3 as these parameters are varied within the following bounds: $P_w/P_k \in [0, 1]$, $R_w/P_k \in [-1, 1]$, $c_3 \in [0, 1]$. We can then further restrict the parameter space by requiring that Ri_f remains realisable ($Ri_f \in [0, 1]$); we are not considering scenarios with global TKE backscatter where $P_k < 0$.

We plot the realisable space of Ri_f values in figure 2 following (2.6) for three different limiting cases: (a) for $P_w/P_k = 0$, corresponding to scenarios that only force the horizontal momentum equations; (b) for $P_w/P_k = 1$, corresponding to scenarios that only force the vertical momentum equations; (c) for $c_3 = 1/3$, corresponding to a large Reynolds number limit where small-scale isotropy is recovered (e.g. in the absence of mean shear, this would require $Re_L \gg 1$ for $Fr_k > 1$ or $Re_b \gg 1$ for $Fr_k \leq 1$); and (d) for $P_w/P_k = 1$ (blue) and $P_w/P_k = 0$ (orange) with $c_3 = 1/3$. The scenarios that involve $0 < P_w/P_k < 1$ sit between the realisable triangular regions in the top left of figure 2(a) and the bottom left of figure 2(b) in the R_w/P_k and c_3 space. Relatedly, in the large Reynolds number limit, the entire realisable space of Ri_f values sit between the two limits of $P_w/P_k = 0$ and $P_w/P_k = 1$ (see the realisable diagonal strip of $0 \leq Ri_f \leq 1$ in figure 2(c), and the space between the blue and orange lines in figure 2d).

While the bounds on Ri_f help constrain the theoretically realisable space of (2.6), Ri_f and the extent of that space are sensitive to how the flow is forced. Flow forcing information can thus further restrict the theoretically realisable space of (2.6) to a smaller space that is empirically observed in measurements or simulations. For example, Yi & Koseff (2023) found larger values of Ri_f for simulations that involved vertical shear ($d_z \bar{u}$) compared with lateral shear ($d_y \bar{u}$) (see their figures 4 and 9b). While these two scenarios obey the same volume-averaged budgets (2.1)–(2.4), they differ in how the pressure–strain redistribution of k_u to k_v and k_w impacts the dynamics (see their figure 10). More generally, to estimate Ri_f for a set of flows that are described by the same volume-averaged budgets, we need to know R_w/P_k , which quantifies how effectively the pressure–strain correlations generate or remove k_w relative to the total mechanical production. Connecting this to the task of parametrising Γ in terms of the governing parameters of stably stratified

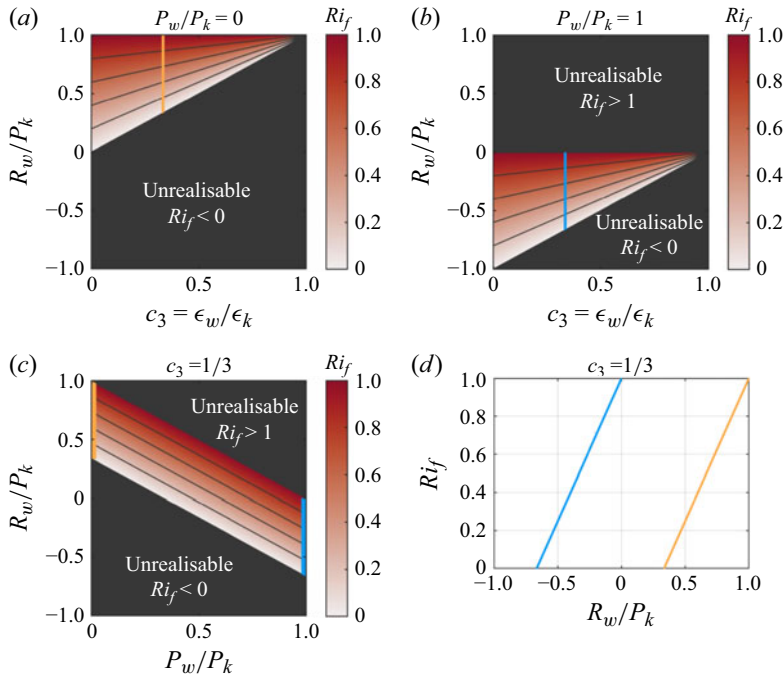


Figure 2. (a,b,c) Contour plots and (d) line plot of the irreversible mixing efficiency $Ri_f = \epsilon_p / (\epsilon_k + \epsilon_p)$ following (2.6) under different limits. Ri_f for (a) $P_w/P_k = 0$, no vertical forcing; (b) $P_w/P_k = 1$, only vertical forcing; (c) $c_3 = 1/3$, large Reynolds number limit (e.g. in the absence of mean shear, this would require $Re_L \gg 1$ for $Fr_k > 1$ or $Re_b \gg 1$ for $Fr_k \leq 1$); (d) $P_w/P_k = 1$ (blue) and $P_w/P_k = 0$ (orange) with $c_3 = 1/3$. The dark contours in the first three panels correspond to $Ri_f = 0.2, 0.4, 0.6$ and 0.8 .

turbulence, this implies that we need to understand how pressure–strain redistribution and dissipation anisotropy depend on (i) how the turbulence is forced and (ii) the range of isotropic and anisotropic scales. In the following sections, we pursue the first goal by developing a better understanding of how two particular pressure correlations (the pressure–strain redistribution and the pressure scrambling terms) change as stability is increased from near neutral to strongly stable conditions and their relationships to Γ . We also briefly touch on the second goal by comparing simulations with strong stability (nominally the same Fr_k) at two different Reynolds numbers, highlighting the multiparameter dependence of Γ that we have discussed here.

3. Description of DNS dataset

In this section, we introduce the dataset and key findings from Yi & Koseff (2022a) to set the stage for the subsequent analyses of the nonlinear and buoyancy pressure correlations.

3.1. Problem set-up and methodology

We revisit the DNS dataset of homogeneous, forced, stably stratified turbulence studied by Yi & Koseff (2022a), which is governed by the incompressible, Navier–Stokes equations under the Boussinesq approximation with linear velocity forcing (Lundgren, T. S. 2003; Rosales & Meneveau 2005):

$$\partial_j u_j = 0, \quad (3.1)$$

$$\partial_t u_j + u_m \partial_m u_j = -\frac{1}{\rho_0} \partial_j p - \frac{g}{\rho_0} \rho \delta_{j3} + \nu \partial_m \partial_m u_j + A u_j, \quad (3.2)$$

$$\partial_t \rho + u_m \partial_m \rho = -w d_z \bar{\rho}_B + D \partial_m \partial_m \rho, \quad (3.3)$$

where u_j , p , ρ represent the velocity, pressure and density fields, respectively; ρ is defined as the perturbation from $\rho_0 + \bar{\rho}_B(z)$, with ρ_0 being the reference density and $\bar{\rho}_B(z)$ being the prescribed, stable, linearly varying background density field ($d_z \bar{\rho}_B < 0$ and constant); g is the gravitational acceleration; ν is the kinematic viscosity of the fluid; D is the molecular diffusivity of density; and A is the momentum forcing rate. A point to highlight is that this momentum forcing is active in all three directions and is proportional to the velocity perturbations in that direction. Imposing a stability that damps w (via the buoyancy force), hence, also reduces $P_w = A w^2$ relative to $P_u = A u^2$ and $P_v = A v^2$, further damping the vertical component. Tensor indices (1, 2, 3) correspond to spatial directions (x , y , z) and velocity fields (u , v , w) with gravity acting along the z -axis. Repeated indices imply summation. Equations (3.1)–(3.3) were solved in a triply periodic, cubic domain of length $L = 2\pi$ using a Fourier pseudospectral solver with a fourth-order Runge–Kutta time-stepping scheme. Nonlinear terms were dealiased exactly by zero-padding (i.e. they are computed using zero-padded arrays of size $3N/2$ and retaining the first N Fourier modes in each dimension). The code has been verified and used in several studies (Yi & Koseff 2022a,b, 2023).

A key strength of using this dataset rather than the three shear-forced datasets studied by Yi & Koseff (2023) is that the linear forcing ($A u_j$) is divergence free, which allows for the pressure fluctuations to be decomposed into just two components associated with the non-divergent parts of the nonlinear and buoyancy terms in (3.2), which will be discussed further in § 4.1.

3.2. Second-moment budgets

Here, we overview the volume-averaged (indicated by overbars) budgets of the turbulent kinetic energy (TKE, $k = (1/2) \overline{u_j u_j}$), turbulent potential energy (TPE, $k_p = (1/2) \alpha^2 \overline{\rho \rho}$), Reynolds stress ($\overline{u_i u_j}$) and buoyancy flux ($B_j = (g/\rho_0) \overline{u_j \rho}$) associated with (3.1)–(3.3). Here, $\alpha = g/(\rho_0 N)$ is a dimensional coefficient used to convert the dimensions of ρ to match those of velocity (and thus convert the density variance into potential energy units). Because the system is axisymmetric about the vertical axis, we simply consider the horizontal and vertical Reynolds stresses (diagonal entries of $\overline{u_i u_j}$) and the vertical buoyancy flux ($B = (g/\rho_0) \overline{w \rho}$). This reduced set of budgets is given as

$$d_t k = \underbrace{2Ak}_{\text{TKE production}} - \underbrace{\frac{g}{\rho_0} \overline{w \rho}}_{\text{vertical buoyancy flux}} - \underbrace{\overline{\nu \partial_m u_j \partial_m u_j}}_{\text{TKE dissipation}} = P_k - B - \epsilon_k, \quad (3.4)$$

$$d_t k_p = \underbrace{\frac{g}{\rho_0} \overline{w \rho}}_{\text{vertical buoyancy flux}} - \underbrace{D \alpha^2 \overline{\partial_m \rho \partial_m \rho}}_{\text{TPE dissipation}} = B - \epsilon_p, \quad (3.5)$$

$$d_t k_H = \underbrace{2Ak_H}_{\text{horizontal TKE production}} + \underbrace{\frac{1}{\rho_0} \overline{p s_{HH}}}_{\text{horizontal pressure-strain}} - \underbrace{\overline{\nu \partial_m u_H \partial_m u_H}}_{\text{horizontal TKE dissipation}} = P_H + R_H - \epsilon_H, \quad (3.6)$$

$$d_t k_w = \underbrace{2Ak_w}_{\text{vertical TKE production}} + \underbrace{\frac{1}{\rho_0} \overline{ps_{33}}}_{\text{vertical pressure-strain}} - \underbrace{\frac{g}{\rho_0} \overline{w\rho}}_{\text{vertical buoyancy flux}} - \underbrace{\nu \overline{\partial_m w \partial_m w}}_{\text{vertical TKE dissipation}} = P_w + R_w - B - \epsilon_w, \quad (3.7)$$

$$\begin{aligned} d_t B &= \underbrace{AB}_{\text{vertical buoyancy flux production by forcing}} + \underbrace{\frac{g}{\rho_0^2} \overline{p \partial_z \rho}}_{\text{vertical pressure scrambling}} + \underbrace{2N^2(k_w - k_p)}_{\text{source/sink due to } k_w \text{ and } k_p} - \underbrace{(\nu + D) \left(\frac{g}{\rho_0} \right) \overline{\partial_m w \partial_m \rho}}_{\text{vertical buoyancy flux dissipation}} \\ &= P_B + R_B + 2N^2(k_w - k_p) - \epsilon_B. \end{aligned} \quad (3.8)$$

Equations (3.4) and (3.5) are the volume-averaged kinetic and potential energy budgets, where P_k is the production rate of TKE by the linear forcing term; B is the vertical buoyancy flux that here converts TKE to TPE; and ϵ_k and ϵ_p are the dissipation rates of TKE and TPE, respectively. Equations (3.6) and (3.7) are the volume-averaged budgets for the horizontal and vertical components of TKE ($k_H = (1/2)\overline{u_H u_H} = (1/2)(1/2\overline{uu} + (1/2)\overline{vv})$; $k_w = (1/2)\overline{ww}$), where adding two times (3.6) with (3.7) results in (3.4) ($k = 2k_H + k_w$). The sources and sinks in these equations are as follows: $P_H = (A/2)(\overline{uu} + \overline{vv})$ and P_w are the production rates of the horizontal and vertical components of TKE; $R_H = (1/2\rho_0)(\overline{ps_{11}} + \overline{ps_{22}})$ and R_w are the pressure–strain correlations, which sum to zero (i.e. $2R_H = -R_w$) due to the incompressibility condition (3.1); and $\epsilon_H = (\nu/2)(\overline{\partial_m u_1 \partial_m u_1} + \overline{\partial_m u_2 \partial_m u_2})$ and ϵ_w are the dissipation rates of the horizontal and vertical components of TKE. Equation (3.8) is the volume-averaged budget for the vertical buoyancy flux, where P_B is a source term due to forcing (equivalent to production by the mean-velocity gradient in stratified wall-bounded flows); R_B is the pressure scrambling term; $2N^2 k_w$ is a source due to k_w (equivalent to production by the mean-density gradient in stratified wall-bounded flows); $-2N^2 k_p$ is a sink due to k_p (equivalent to buoyant destruction in stratified wall-bounded flows); and ϵ_B is a ‘dissipation’ term for vertical buoyancy flux (this term, however, is not sign definite). The transport terms are exactly zero because our flow is statistically homogeneous in all three spatial directions, which is why only the volume-averaged sources and sinks remain in (3.4)–(3.8).

3.3. Reynolds stress and buoyancy flux budgets and their relationship with mixing coefficient

We can visualise the energy exchange in our system under statistically stationary conditions following (3.5)–(3.7). In figure 3, ingoing arrows indicate sources and outgoing arrows indicate sinks of each of the three energy buckets. Forcing directly produces k_H and k_w (black arrows). There is also intercomponent exchange by pressure–strain redistribution, which under stable conditions, and with the three-dimensional forcing in our DNS, will convert k_H into k_w to reduce the large-scale anisotropy due to buoyancy effects (blue arrow). (Note that the conversion would have been from k_w to k_H for cases with $P_w/P_k = 1$ as discussed in the previous section.) The buoyancy flux converts k_w into k_p (orange arrow) and, finally, there are dissipative losses (red arrows).

Before presenting the key results, we first illustrate the parameter space spanned by the DNS dataset of Yi & Koseff (2022a) by plotting the volume- and time-averaged values of Re_L and Fr_k from the 42 simulations in this dataset in figure 4 (purple circles). Lines of constant $Re_b = Re_L Fr_k^2$ are marked by the diagonal dashed lines (increasing in order of magnitude from 1 to 10^4). The dataset spans roughly three orders of magnitude in Fr_k , covering near neutral to very strongly stable conditions. The simulations with $Fr_k > 1$ have

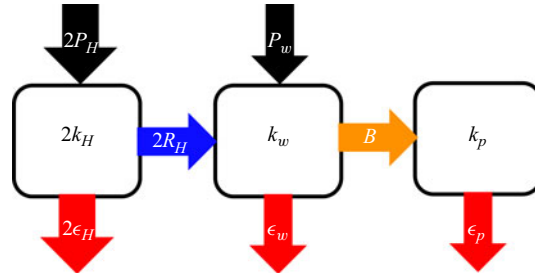


Figure 3. Energy exchange diagrams under the statistically stationary conditions of our DNS set-up, following (3.5)–(3.7). Ingoing arrows indicate sources and outgoing arrows indicate sinks of the three energy buckets (horizontal and vertical components of TKE and TPE). Black arrows indicate direct production by the forcing term, the blue arrow indicates the pressure–strain redistribution term, the orange arrow indicates the vertical buoyancy flux and red arrows indicate the dissipation terms.

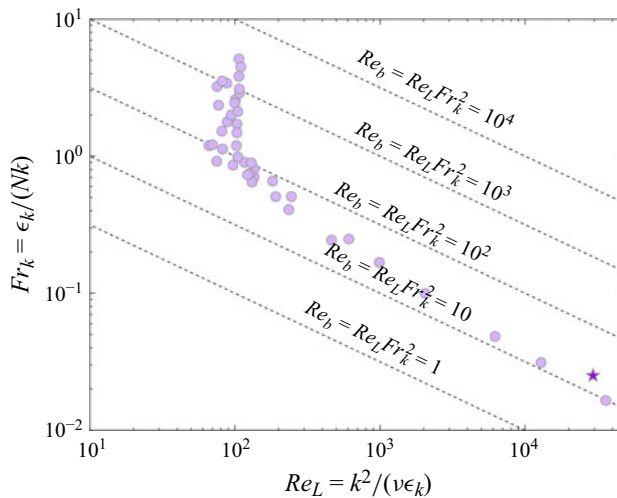


Figure 4. Volume- and time-averaged values of Re_L and Fr_k from the DNS dataset of Yi & Koseff (2022a) (purple circles) and an additional higher Reynolds number simulation at strong stability (purple star).

$Re_L \approx 100$, whereas the simulations with $Fr_k \leq 1$ have Re_b between 10 and 100, where Re_b decreases for simulations with smaller values of Fr_k as a wider range of anisotropic scales are simulated at the expense of isotropic scales. We choose to plot the results as a function of Fr_k for simplicity and continuity with how they are originally presented by Yi & Koseff (2022a), but we should note that Reynolds number variations do affect the quantities of interest as we have discussed in § 2. To illustrate this multiparameter dependence, we also present the results from a higher Reynolds number simulation with strong stability ($Fr_k \sim \mathcal{O}(10^{-2})$) (purple star). Key simulation input and output parameters are summarised in table 1 with C-series simulations involving a fixed value of the forcing coefficient A in time, whereas the K-, D- and V-series simulations involve time-varying values of A to maintain specific values of k , ϵ_k and k_w , which are reported in the table. The time-varying forcing approach builds on that of Bassenne *et al.* (2016), and the details of how $A(t)$ is chosen can be found in Appendix B of Yi & Koseff (2022a). A key benefit of this time-varying forcing scheme is that the simulations more rapidly reach statistically stationary conditions relative to a constant forcing scheme. We illustrate this benefit further

Sim.	A/N	Fr_k	Re_L	Re_b	k	ϵ_k	k_w	P_w/P_k	R_w/P_k	c_3	Ri_f
C1	0.3750	0.6586	181.91	75.81	7.61	6.74	1.37	0.1804	0.2061	0.2716	0.14646
C2	0.5000	0.8595	97.09	71.32	4.13	3.57	0.93	0.2253	0.1779	0.2933	0.15068
C3	0.9300	1.7172	103.36	302.71	5.85	6.73	1.66	0.2829	0.0859	0.3134	0.07901
C4	1.3578	2.5870	100.96	669.90	6.20	7.68	1.88	0.3028	0.0500	0.3235	0.04463
C5	1.4895	2.8869	107.47	887.94	6.71	8.45	1.99	0.2964	0.0496	0.3228	0.03429
C6	1.9500	3.8211	106.57	1544.02	6.73	8.58	2.12	0.3149	0.0276	0.3270	0.02328
C7	2.2768	4.4771	109.85	2181.21	6.95	8.89	2.22	0.3193	0.0217	0.3304	0.01681
C8	2.6000	5.1262	106.55	2775.85	6.77	8.67	2.25	0.3325	0.0082	0.3308	0.01451
K1	0.4155	0.7031	135.63	63.28	6.0	5.63	1.17	0.2005	0.1862	0.2767	0.15369
K2	0.5215	0.9010	116.79	91.90	6.0	6.36	1.32	0.2244	0.1645	0.2929	0.13543
K3	0.6405	1.1267	82.21	101.40	3.0	2.25	0.71	0.2418	0.1343	0.2911	0.11977
K4	0.6719	1.1936	102.50	143.23	6.0	7.16	1.48	0.2484	0.1320	0.3026	0.11144
K5	0.8155	1.4824	103.29	222.36	6.0	7.12	1.59	0.2682	0.1030	0.3082	0.09095
K6	1.2506	2.3540	77.17	423.73	3.0	2.35	0.87	0.2919	0.0682	0.3204	0.06936
K7	1.2831	2.4412	99.75	585.89	6.0	7.32	1.81	0.3027	0.0551	0.3245	0.04858
K8	1.6597	3.2197	75.43	772.73	3.0	2.41	0.91	0.3049	0.0384	0.3227	0.03002
D1	0.1500	0.2438	463.70	22.50	6.61	2.00	0.57	0.0903	0.2253	0.1706	0.17831
D2	0.2504	0.4070	234.90	33.75	5.80	3.00	0.78	0.1387	0.2292	0.2307	0.18025
D3	0.3071	0.5071	190.88	45.00	6.10	4.00	0.93	0.1549	0.2169	0.2484	0.16786
D4	0.3031	0.5073	245.21	60.00	9.50	7.50	1.46	0.1555	0.2234	0.2569	0.16267
D5	0.3927	0.6461	131.32	50.63	5.36	4.50	1.07	0.2010	0.1984	0.2748	0.17390
D6	0.4291	0.7308	122.34	60.00	5.17	4.50	1.04	0.2055	0.1908	0.2782	0.15750
D7	0.4455	0.7468	126.11	67.50	6.11	6.00	1.30	0.2138	0.1856	0.2870	0.15988
D8	0.4746	0.8056	135.69	84.38	7.08	7.50	1.48	0.2103	0.1760	0.2855	0.14617
D9	0.5179	0.8920	129.84	100.00	6.94	7.50	1.53	0.2213	0.1638	0.2888	0.13988
D10	0.5322	0.9196	74.90	60.00	2.35	1.50	0.52	0.2240	0.1610	0.2761	0.14502
D11	0.5690	0.9878	104.78	100.00	4.84	4.50	1.12	0.2318	0.1557	0.2942	0.13430
D12	0.6815	1.1967	66.32	91.88	2.22	1.50	0.56	0.2522	0.1274	0.2943	0.12154
D13	0.6829	1.2121	69.93	100.00	2.28	1.50	0.54	0.2370	0.1359	0.2952	0.11269
D14	0.8448	1.5227	81.29	183.75	3.48	3.00	0.96	0.2756	0.0977	0.3067	0.09725
D15	0.9639	1.7820	88.65	275.63	4.45	4.50	1.24	0.2794	0.0841	0.3120	0.07471
D16	1.0709	1.9989	94.36	367.50	5.30	6.00	1.53	0.2889	0.0753	0.3196	0.06601
D17	1.1213	2.1152	104.64	459.38	6.24	7.50	1.77	0.2846	0.0727	0.3182	0.05720
D18	1.5926	3.0912	107.12	1000.02	6.31	7.50	1.93	0.3067	0.0389	0.3251	0.03220
D19	1.7539	3.4170	87.71	1000.00	4.42	4.50	1.36	0.3099	0.0339	0.3264	0.02807
D20	1.8112	3.5333	81.79	1000.00	3.49	3.00	1.08	0.3100	0.0351	0.3276	0.02679
V1	0.0093	0.0165	35933.73	9.83	295.98	49.15	1.30	0.0045	0.1148	0.0409	0.08334
V2_128	0.0146	0.0251	29340.94	18.32	121.39	20.36	1.30	0.0107	0.2389	0.1190	0.14735
V2	0.0180	0.0312	12862.77	12.40	132.22	27.55	1.30	0.0099	0.1561	0.0662	0.10922
V3	0.0284	0.0484	6201.62	14.06	73.13	17.58	1.30	0.0179	0.1855	0.0882	0.13128
V4	0.0600	0.0997	2044.58	18.65	31.75	10.36	1.30	0.0420	0.2266	0.1380	0.15450
V5	0.1030	0.1678	989.35	25.60	19.53	8.00	1.30	0.0686	0.2445	0.1761	0.17032
V6	0.1532	0.2485	609.54	36.11	14.65	7.22	1.30	0.0900	0.2446	0.2013	0.17261

Table 1. Volume- and time-averaged input and output parameters for the simulations. The C-series simulations involve a fixed value of A in time, whereas the K-, D- and V-series simulations involve time-varying values of A to maintain specific values of k , ϵ_k and k_w , respectively, which are provided in the table. All simulations used $N = 64$ Fourier modes in each spatial direction, except for simulation V2_128, which used $N = 128$ modes. The C-, K- and D-series simulations all had values of $\kappa_{max}\eta \approx 2$, whereas the lowest value for the V-series simulations was $\kappa_{max}\eta \approx 1.25$.

in relation to the growth of energy in large horizontal-scale motions termed ‘shear modes’ in strongly stable, forced turbulence simulations in [Appendix A](#).

Next, we consider the volume-averaged budgets of the horizontal and vertical components of the TKE (k_H and k_w), and the vertical buoyancy flux (B) as a function of the turbulent Froude number (Fr_k) in [figure 5\(a,b,d\)](#). We also connect these budgets to the relationship between the mixing coefficient (Γ) and Fr_k in [figure 5\(c\)](#). In the following paragraphs, we denote weak stratification where we observe monotonic increase

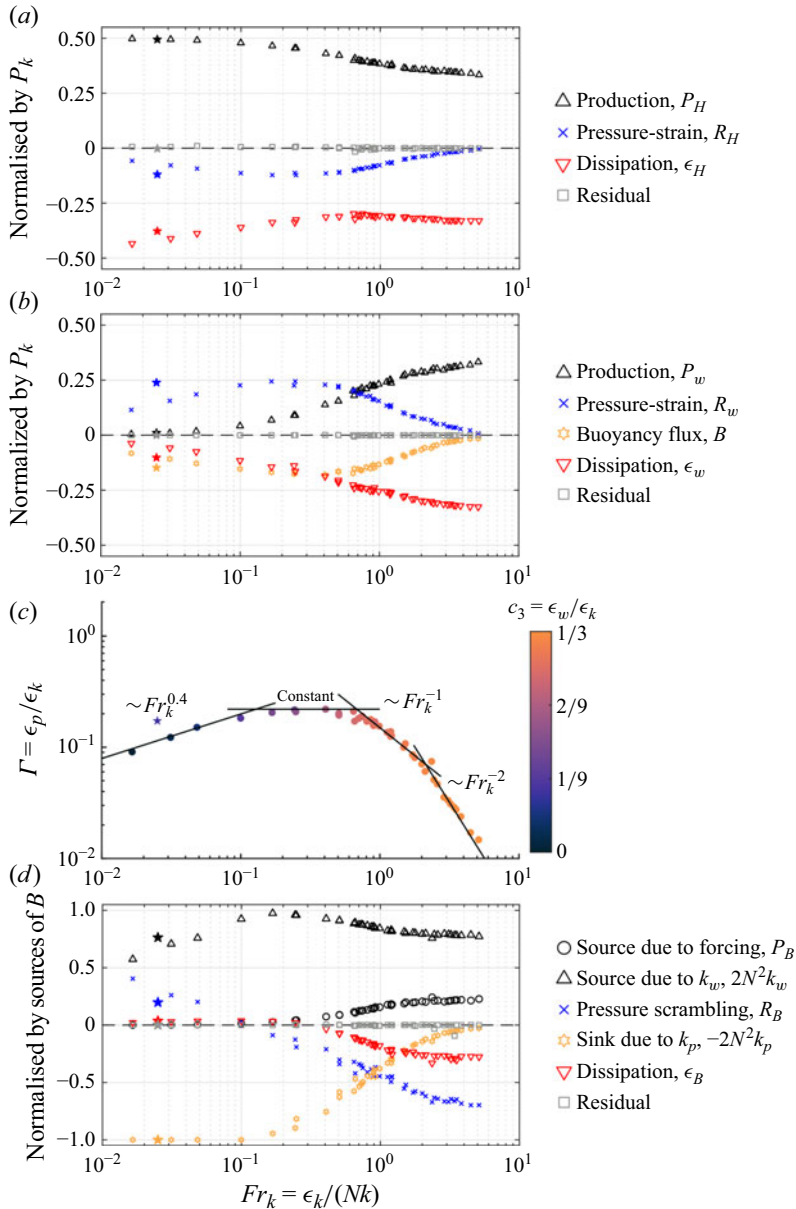


Figure 5. Steady-state, volume- and time-averaged budgets of (a) k_H , (b) k_w and (d) B as a function of the turbulent Froude number (Fr_k). The three panels correspond to (3.6)–(3.8). The mixing coefficient Γ is plotted in panel (c) as a function of Fr_k with the dissipation anisotropy factor $c_3 = \epsilon_w / \epsilon_k$ shown in colour. The results from the higher Reynolds number simulation (V2_128) are denoted by filled stars.

of R_w / P_k (relative importance of pressure–strain redistribution of k_w to total mechanical production), moderate stratification where R_w / P_k plateaus along with Γ , and strong stratification where pressure scrambling (source/sink in the vertical buoyancy flux budget) becomes positive and where Γ begins to decrease. These choices are made given that the specific Fr_k thresholds associated with these dynamical changes in the volume-averaged budgets will be sensitive to how the turbulence is forced and the Reynolds number.

In figures 5(a) and 5(b), we plot the steady-state, volume- and time-averaged budgets of k_H and k_w normalised by the total production of TKE (P_k). First, we consider the budget for k_H (figure 5a). When stratification is weak (large Froude numbers), the pressure–strain correlation is weak (blue exes), and there is a balance between production and dissipation (black and red triangles). As stratification increases (moving from large to small Froude numbers), production of k_H increases in magnitude relative to total production (black triangles) since k_H becomes larger than k_w due to damping by buoyancy and consequent reduced production of the latter. With this change, the pressure–strain correlation becomes a sink of k_H , and it reaches a plateau around $Fr_k \approx 0.7$ before starting to decrease in magnitude for $Fr_k < 0.1$. Dissipation of k_H initially becomes smaller until $Fr_k \approx 0.7$ before increasing in magnitude for $Fr_k < 0.7$.

Next, we consider the budget for k_w (figure 5b). Like with k_H , when stratification is weak (large Froude numbers), the pressure–strain correlations (blue exes) and buoyancy flux (orange stars) are negligible, and there is a balance between production and dissipation. As stratification increases (moving from large to small Froude numbers), vertical motions are damped by buoyancy ($k_w < k_H$) and direct production of k_w decreases. As large-scale anisotropy becomes important in the system, the pressure–strain correlation becomes a source of k_w , increasing in magnitude until reaching a plateau at $Fr_k \approx 0.7$ before decreasing for $Fr_k < 0.1$. Relatedly, the buoyancy flux increases in magnitude until $Fr_k \approx 0.7$, overtaking dissipation as the main sink of k_w , before sharply decreasing in magnitude for $Fr_k < 0.1$. Dissipation of k_w decreases as stratification is increased.

In figure 5(d), we plot the steady-state, volume- and time-averaged budget of the vertical buoyancy flux ($B = (g/\rho_0)\overline{w\rho}$) as a function of the turbulent Froude number (Fr_k). The terms have been normalised by the sum of all source terms to keep their values in the range of ± 1 . When stratification is weak (large Froude numbers), the buoyancy flux is generated primarily by the source due to k_w (black triangles) and secondarily by the source due to forcing (black circles), and it is destroyed primarily by pressure scrambling (blue exes) and secondarily by dissipation (red triangles). As stratification increases (moving from large to small Froude numbers), the source due to forcing and the dissipation weaken, and a dominant balance between three terms arises: generation by source due to k_w , destruction by pressure scrambling, and sink due to k_p (orange stars). When $Fr_k \approx 0.1$, the pressure scrambling term becomes negligible, and there is a balance between source due to k_w and sink due to k_p . However, as stratification increases further ($Fr_k < 0.1$), the source due to k_w weakens, and pressure scrambling switches signs and begins to generate buoyancy flux to ensure that the buoyancy flux remains positive, which is expected for stably stratified systems. The emerging dominant balance as one goes to even lower Fr_k than we simulated seems to be between the pressure scrambling term correlating vertical velocity and density to produce buoyancy flux and buoyancy destruction working to reduce the correlation and flux. This balance also emerged in DNS of stably stratified wall-bounded flow away from the wall and at high stabilities reported by Shah & Bou-Zeid (2014) (see their figure 20d for $Ri_b = 0.968$).

Finally, in figure 5(c), we plot the mixing coefficient (Γ) as a function of Fr_k with the dissipation anisotropy factor $c_3 = \epsilon_w/\epsilon_k$ from § 2 shown in colour. Doing so illustrates how the range of isotropic scales vary simultaneously with Fr_k , highlighting the multiparameter variations that occur across the set of simulations (see figure 4). Because we keep the simulation resolution fixed while varying the stability in the original set of simulations (circles), an increasing range of anisotropic scales are simulated at the cost of decreasing range of isotropic scales, which explains why simulations with weak

stability have values of c_3 close to $1/3$ (indicating small-scale isotropy), while simulations with stronger stability have systematically smaller values of c_3 (indicating departures from small-scale isotropy). The three rightmost scaling regimes ($\Gamma \sim Fr_k^{-2}$, $\Gamma \sim Fr_k^{-1}$ and $\Gamma \approx \text{constant}$) have been theoretically discussed by Garanaik & Venayagamoorthy (2019), but the leftmost scaling of $\Gamma \sim Fr_k^{0.4}$ is an empirical fit to the results of simulations V1, V2, V3 and V4 (four leftmost circles). The deviation of the higher Reynolds number simulation (filled star) is discussed in the subsequent paragraph. As stratification increases, Γ increases until it plateaus at a value of $\Gamma \approx 0.2$ for $Fr_k \approx 0.7$. This coincides with when the pressure–strain redistribution becomes equally important in generating k_w and reaches a plateau (figure 5b). As stratification increases further, $\Gamma \approx 0.2$ is maintained until $Fr_k < 0.1$ when it begins to decrease. This is connected with a decrease in the pressure–strain redistribution, which is the main mechanism for generating k_w for $Fr_k < 0.1$, and there is an accompanied decrease in the vertical buoyancy flux (figure 5b). As redistribution from k_H to k_w weakens, leading to a diminished vertical buoyancy flux, we observe in the vertical buoyancy flux budget that the source due to k_w term diminishes in magnitude relative to the sink due to k_p term, and the pressure scrambling term changes sign and becomes a source of vertical buoyancy flux (figure 5c).

We note that increasing the Reynolds number while keeping stability relatively fixed (e.g. compare simulations V2 and V2_128, corresponding to $Fr_k \approx 0.031$ and $Fr_k \approx 0.025$, respectively; results from simulation V2_128 are denoted by filled stars) results in a more effective pressure–strain redistribution from k_H to k_w and weakens the loss of k_H by dissipation (figure 5a). This more effective generation of k_w is accompanied by greater losses via enhanced conversion of k_w into k_p by the buoyancy flux and viscous dissipation (figure 5b). Regarding the larger buoyancy fluxes associated with increasing Reynolds number, we observe that this change is associated with a relative strengthening of the source due to k_w compared with pressure scrambling, which is due to the greater conversion of k_H into k_w by more effective pressure–strain redistribution (figure 5d). These changes result in a greater value of Γ as the Reynolds number is increased (figure 5c), which can be explained by considering (2.6). We find that increasing the Reynolds number while keeping stability relatively fixed results in (i) negligible changes to the fraction of the TKE production that directly generates k_w (P_w/P_k remains largely unchanged), (ii) enhanced pressure–strain redistribution into k_w relative to TKE production (R_w/P_k increases) and (iii) more of the TKE loss occurring via dissipative losses of k_w (c_3 increases). Visually, we can see this by considering figure 2(a) (note that $P_w/P_k \sim \mathcal{O}(10^{-2})$ for simulations V2 and V2_128), where simultaneous increases in R_w/P_k and c_3 result in larger values of $\Gamma = Ri_f/(1 - Ri_f)$ (i.e. movement towards the top right corner of the realisable region that is left of the orange vertical line). Regarding the transition between $\Gamma \approx \text{constant}$ and $\Gamma \sim Fr_k^{0.4}$, we note that the latter relationship is an empirical fit that needs to be revisited based on simulations that vary Fr_k while keeping Re_b fixed, which would reveal the relationship between Γ and Fr_k at strong stability for different values of c_3 .

Bou-Zeid *et al.* (2018) in studying the relationship between Ri_f and the gradient Richardson number ($Ri_g = N^2/S^2$) observed a similar relationship where Ri_f first increases with Ri_g (increasing stability), but then reaches a plateau, where the former regime was referred to as the ‘ B -limited regime’, indicating a limitation in the magnitude of the vertical buoyancy flux due to the background density gradient and its ability to convert TKE to TPE, and the latter regime was referred to as the ‘ R_w -limited regime’, indicating a limitation in the magnitude of the vertical buoyancy flux due to the pressure-redistribution term. These ideas are connected with the left and right flanks of the

relationship between Γ and Ri_g as described by Caulfield (2021). The results from the higher Reynolds number simulation at strong stability highlights the need to explore the effects of Reynolds number in both the ‘ B -limited regime’ and the ‘ R_w -limited regime’ for a more complete physical understanding of mixing associated with stably stratified turbulence.

In this section, we have summarised the key findings of Yi & Koseff (2022a), connecting the shape of Γ as a function of some measure of dynamic stability (here we have used Fr_k) to changes in the generation of k_w by pressure–strain redistribution and the associated change in the generation of B by the pressure scrambling term for very strong stability. We also briefly explored the role of the Reynolds number through an additional simulation, which (when combined with our analysis in § 2) suggests that greater values of Γ will result when Reynolds number is increased while keeping Fr_k fixed for strong stability. Given that Yi & Koseff (2023) also reported sign changes of the pressure scrambling terms at strong stability for three different types of shear-forced, stably stratified turbulence simulations, we attempt to explain this seemingly more general feature of stably stratified turbulence in the next section by further studying these two pressure-related quantities.

4. Analysis of pressure correlations

4.1. Pressure decomposition

To diagnose these pressure effects further, we consider the Poisson equation governing the pressure fluctuations by taking the divergence of (3.2),

$$\partial_j \partial_j p = -\rho_0 \partial_j u_m \partial_m u_j - g \partial_z \rho. \quad (4.1)$$

We then decompose the pressure fluctuations into nonlinear and buoyancy components (p_{NL} and p_B) that separately satisfy the two right-hand side source terms:

$$\partial_j \partial_j p_{NL} = -\rho_0 \partial_j u_m \partial_m u_j, \quad (4.2)$$

$$\partial_j \partial_j p_B = -g \partial_z \rho. \quad (4.3)$$

As mentioned in § 3, the shear-forced datasets of Yi & Koseff (2023) involve an additional right-hand side term in (4.1) due to the non-divergence of the shear forcing terms. This would require solving for a third set of pressure fluctuations associated with the terms involving the mean shear. The current dataset, however, allows us to study just the competition between the nonlinear and buoyancy components of the pressure fluctuations. When running the DNS, we solved the full Poisson equation for the pressure (4.1). Here, we separately compute p_{NL} and p_B offline as a postprocessing step to probe their responses to increasing stability.

In figure 6(a), we plot the normalised pressure variance as a function of the turbulent Froude number (Fr_k). With $p = p_{NL} + p_B$, the volume-averaged pressure variance is $\overline{p^2} = \overline{p_{NL}^2} + \overline{p_B^2} + 2\overline{p_{NL}p_B}$. The total pressure variance (blue exes) has been plotted using the sum of the three right-hand side terms to verify the offline postprocessing of the nonlinear and buoyancy components of the pressure fluctuations. The total pressure variance is dominated by the nonlinear component (purple squares), but the buoyancy component (blue circles) increases in magnitude with stability. The nonlinear and buoyancy components are anticorrelated, and this anticorrelation strengthens with stability (orange triangles).

Next, we consider the normalised pressure–strain correlations (R_w/P_k) in figure 6(b), which at its peak amounts to $\sim 25\%$ of the TKE production. Recall that positive values

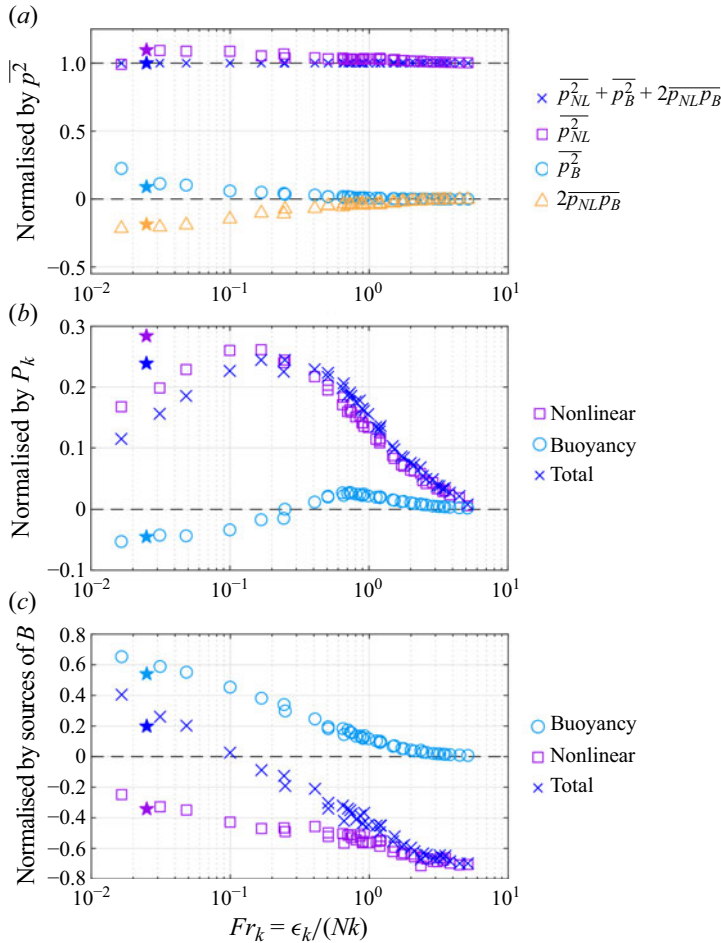


Figure 6. Normalised (a) pressure variance, (b) pressure–strain correlation and (c) pressure scrambling term as a function of Fr_k . The results from the higher Reynolds number simulation (V2_128) are denoted by filled stars.

indicate transfer of k_H into k_w and negative values indicate transfer of k_w into k_H . For weak stratification, the nonlinear component makes up most of the pressure–strain correlations, but the total contribution of the pressure–strain term to the dynamics is small since the turbulence is nearly isotropic in these simulations. The buoyancy component increases with stratification until $Fr_k \approx 0.7$, contributing to the redistribution of energy from k_H into k_w , which promotes large-scale return-to-isotropy. For $Fr_k < 0.7$, however, the buoyancy component begins to decrease and eventually changes sign for $Fr_k \approx 0.3$, becoming a sink of k_w . This conversion from vertical to horizontal TKE goes counter to the return-to-isotropy expectation as it redistributes energy from the less energetic component k_w (that in our simulations still has a source associated with the forcing) to the more energetic ones k_H . We find that the decrease in the total pressure–strain correlation for $Fr_k < 0.1$ is driven by both a weaker exchange of k_H into k_w by the nonlinear component and a stronger exchange of k_w into k_H by the buoyancy component. Interestingly, when considering the higher Reynolds number simulation with $Fr_k \approx 0.025$, we note that while the buoyancy pressure–strain redistribution maintains a similar magnitude

as the lower Reynolds simulation with $Fr_k \approx 0.031$, we observe that the net pressure-strain redistribution increases by approximately 50 % due to a significant increase of the nonlinear component. We additionally note that this significant change in the correlation is associated with relatively negligible differences of the pressure variance components between the lower and higher Reynolds number simulations (figure 6a).

Finally, we consider the normalised pressure scrambling term in figure 6(c). For weak stratification, the nonlinear component makes up most of the pressure scrambling term and represents a large negative fraction (approximately -70 %) of the total production of covariance. Therefore, the total pressure scrambling term acts as a sink of vertical buoyancy flux. However, as stratification increases, the nonlinear component begins to weaken, and this is accompanied by a largely monotonic increase of the buoyancy component. Focusing on very strong stratification ($Fr_k < 0.1$), we note that the sign change of the total pressure scrambling term is due to the compensation between the nonlinear and buoyancy components, and as the buoyancy component of the pressure scrambling term starts to dominate, the total pressure scrambling term becomes an increasingly important means of generating vertical buoyancy flux (see also figure 5d). Comparing the lower and higher Reynolds number simulations ($Fr_k \approx 0.031$ and $Fr_k \approx 0.025$), we observe that the nonlinear component of the pressure scrambling increases slightly in magnitude while the buoyancy component of the pressure scrambling decreases in magnitude, leading to a 24 % reduction in the net pressure scrambling term.

4.2. Interpreting the nonlinear and buoyancy pressure fluctuations and their correlations

To develop an understanding of the nonlinear and buoyancy pressure fluctuations, we return to (4.2) and (4.3), which relate the Laplacian of the nonlinear and buoyancy pressure fluctuations to their respective right-hand side source terms ($f_{NL}(\mathbf{x}, t) = -\rho_0 \partial_j u_m \partial_m u_j$ and $f_B(\mathbf{x}, t) = -g \partial_z \rho$). Because our problem set-up is triply homogeneous, the flow variables can be represented as a sum of Fourier modes (denoted by the circumflex symbol), the Fourier coefficients of $\partial_j \partial_j p$ are given by $-\kappa^2 \hat{p}(\boldsymbol{\kappa})$ with $\boldsymbol{\kappa}$ being the wavenumber vector and κ^2 being the squared wavenumber magnitude. Therefore, we can express the Fourier coefficients of the nonlinear and buoyancy components of the pressure fluctuations as $\hat{p}_{NL}(\boldsymbol{\kappa}, t) = -\hat{f}_{NL}/\kappa^2$ and $\hat{p}_B(\boldsymbol{\kappa}, t) = -\hat{f}_B/\kappa^2$, where $\hat{f}_{NL}(\boldsymbol{\kappa}, t)$ and $\hat{f}_B(\boldsymbol{\kappa}, t)$ are the Fourier coefficients of f_{NL} and f_B . One additional constraint on the pressure fields is that their volume-average values are zero, which requires $\hat{p}_{NL}(\boldsymbol{\kappa} = 0, t) = 0$ and $\hat{p}_B(\boldsymbol{\kappa} = 0, t) = 0$.

Relatedly, we can also consider this relationship between the right-hand side terms of (4.2) and (4.3) and the pressure fluctuations in physical space. By using Green's function for the 3-D Poisson equation, we can write the pressure fluctuations as

$$p_{NL}(\mathbf{x}, t) = \iiint -\frac{f_{NL}(\mathbf{x}', t) - \bar{f}_{NL}(t)}{4\pi|\mathbf{x}' - \mathbf{x}|} d\mathbf{x}', \quad (4.4)$$

$$p_B(\mathbf{x}, t) = \iiint -\frac{f_B(\mathbf{x}', t) - \bar{f}_B(t)}{4\pi|\mathbf{x}' - \mathbf{x}|} d\mathbf{x}', \quad (4.5)$$

which involve convolution integrals of Green's function $-1/(4\pi r)$ (r is the distance between two points marked by \mathbf{x} and \mathbf{x}') and the two right-hand side source terms with their volume-averaged values subtracted, $f_{NL} - \bar{f}_{NL}$ and $f_B - \bar{f}_B$, which is necessary to ensure a zero volume-average for the pressure fields. The pressure fields are defined using convolution integrals of the right-hand side terms with the Green's function because

they are governed by elliptic partial differential equations (PDEs), where the pressure at some point \mathbf{x} depends on the values of the right-hand side terms over the whole domain. We note that by the convolution theorem, we can also arrive at $\hat{p}_{NL}(\boldsymbol{\kappa}, t) = -\hat{f}_{NL}/\kappa^2$ and $\hat{p}_B(\boldsymbol{\kappa}, t) = -\hat{f}_B/\kappa^2$ from (4.4) and (4.5), where the Fourier coefficients of Green's function are $-1/\kappa^2$.

Next, we make one final manipulation to f_{NL} by re-expressing it using the rate-of-strain and rate-of-rotation tensors so that $\partial_j u_m = S_{mj} + R_{mj}$ and $\partial_m u_j = S_{jm} + R_{jm}$. With these substitutions, we find

$$f_{NL} = -\rho_0 \partial_j u_m \partial_m u_j = -\rho_0 (S_{jm} S_{jm} - R_{jm} R_{jm}) = -\rho_0 \left(S_{jm} S_{jm} - \frac{1}{2} \omega_q \omega_q \right), \quad (4.6)$$

where we have simplified two terms by noting that a double contraction of symmetric and anti-symmetric tensor sums to zero, and rewriting the rate-of-rotation tensor in terms of the vorticity vector (see a discussion of this decomposition and its relation to the nonlinear pressure fluctuations by Vlaykov & Wilczek 2019). We also note that

$$\overline{f_{NL}} = \rho_0 \left(\frac{1}{2} \overline{\omega_q \omega_q} - \overline{S_{jm} S_{jm}} \right) = 0, \quad (4.7)$$

since $(1/2) \overline{\omega_q \omega_q} = (1/2) \overline{(\partial_j u_i \partial_j u_i)} = \overline{S_{jm} S_{jm}}$ for homogeneous turbulence (see the discussion of pseudo and true dissipation in § 5.3 of Pope 2000).

Here, we briefly summarise the motivation for taking the above-stated steps. We are seeking to understand the pressure-strain and pressure scrambling terms, which requires us to first understand what causes the pressure fluctuations in our problem. To do this, we considered the pressure Poisson equation given in (4.1). If the right-hand side source terms only involve a single Fourier mode, it is possible to state that the pressure fluctuations scale proportionally to the right-hand side terms following $-\partial_j \partial_j p \propto p \propto -f$, but because the right-hand side source terms consist of contributions from a range of scales for turbulent flows, this statement cannot be applied generally in physical space. Rather, we have to resort to the exact relationship between the pressure fields and the right-hand side terms of (4.1) by considering the Green's function solution for the pressure fluctuations ((4.2) and (4.3)), which led to (4.4) and (4.5) that involve convolution integrals of the right-hand side terms of (4.1) with a weighting factor that drops off as $1/r$. Through the convolution theorem, these non-local products in physical space can be stated as local products in Fourier space ($\hat{p}_{NL}(\boldsymbol{\kappa}, t) = -\hat{f}_{NL}/\kappa^2$ and $\hat{p}_B(\boldsymbol{\kappa}, t) = -\hat{f}_B/\kappa^2$), where the factor of $1/\kappa^2$ indicates that larger scales of the right-hand side terms contribute more significantly to the pressure fluctuations than smaller scales. Next, we noted that the volume average of f_{NL} is zero (and so is the volume average of $\partial_z \rho$ due to statistical homogeneity of the density fluctuations in the constant mean density gradient simulations analysed here). Finally, given that the convolution integrals ((4.4) and (4.5)) filter the integrands such that the large scales are weighted more favourably (i.e. contribute more to the integral), we can interpret the positive and negative pressure fluctuations as follows:

- (i) nonlinear pressure fluctuations, (a) $p_{NL} > 0$, regions where large-scale weighted strain dominates, (b) $p_{NL} < 0$, regions where large-scale weighted rotation dominates;
- (ii) buoyancy pressure fluctuations, (a) $p_B > 0$, regions where large-scale weighted unstable density gradients dominate, (b) $p_B < 0$, regions where large-scale weighted stable density gradients dominate.

In the next subsection, these interpretations will prove useful in elucidating the physics of the quadrant analyses we perform on the vertical pressure–strain term in (3.7) and the vertical pressure scrambling term in (3.8).

4.3. Quadrant analyses of the buoyancy flux, pressure–strain redistribution and pressure scrambling dynamics

We now proceed to study the vertical density flux ($w\rho$) and the decomposed pressure correlations that can help clarify the flow physics resulting in TKE redistribution in or out of the vertical TKE component ($p_{NL}\partial_z w$, $p_B\partial_z w$) and the generation or destruction of buoyancy flux ($p_{NL}\partial_z \rho$, $p_B\partial_z \rho$) by applying quadrant analyses (e.g. Wallace 2016). For the vertical density flux, quadrants 1 and 3 are associated with down-gradient fluxes, which convert k_w to k_p , and quadrants 2 and 4 are associated with counter-gradient fluxes, which convert k_p to k_w . For the two pressure–strain correlations (with $k_H > k_w$ for our simulations), quadrant 1 and 3 events convert k_H to k_w , promoting large-scale isotropy, whereas quadrant 2 and 4 events convert k_w to k_H , promoting large-scale anisotropy. For the two pressure scrambling terms, quadrant 1 and 3 events generate vertical buoyancy flux, strengthening the conversion of k_w to k_p , whereas quadrant 2 and 4 events destroy vertical buoyancy flux, weakening the conversion of k_w to k_p . We summarise these ideas and provide brief descriptions of these five sets of correlations in table 2.

In figure 7(a,b,c), we consider the joint probability distribution functions (p.d.f.s) of the vertical density flux ($w\rho$) for three different values of Fr_k : weakest stability $Fr_k \approx 5.13$, where B is negligible and pressure scrambling is negative; strong stability $Fr_k \approx 0.25$, where B is still near its maximum but pressure scrambling is zero; and strongest stability $Fr_k \approx 0.016$, where B has started to diminish and pressure scrambling is positive. The dark contours correspond to the five p.d.f. values ranging between 10^{-1} and 10^{-5} , with one decade spacing in between. The x - and y -axis variables are normalised by the root-mean-squared (r.m.s.) values from each simulation.

For stably stratified turbulence, the averaged vertical buoyancy flux $B = (g/\rho_0)\overline{w\rho}$ is expected to be positive, indicating a net conversion of k_w to k_p (the positive sign can be rationalised through an analogous argument typically used to explain why the Reynolds shear stress $\overline{uw} < 0$ for sheared flows; see also the orange stars in figure 5b). In line with this, we observe that the two variables are positively correlated with down-gradient fluxes (quadrants 1 and 3) occurring more frequently than counter-gradient fluxes (quadrants 2 and 4), as indicated by the larger probability mass contained in the down-gradient flux quadrants than in the counter-gradient flux quadrants (see the text near the four corners). As stability increases (left to right), we observe that counter-gradient fluxes occur more often, and the overall correlation weakens (inner p.d.f. contours become more circular). Since counter-gradient buoyancy fluxes represent parcels returning towards their equilibrium elevation (where the mean density is equal to that parcel density), when there is weak mixing, enhanced counter-gradient fluxes result in weaker correlation between w and ρ and implies weaker vertical exchange of buoyancy.

Another way to explain this phenomenon is to consider the turbulent Froude number as a ratio of two time scales $Fr_k = \epsilon/(Nk) \sim \tau_B/\tau_L$, where $\tau_B \sim 1/N$ is the buoyancy time scale characterising the reversible exchange between k_w and k_p associated with density perturbations, and $\tau_L \sim k/\epsilon_k$ is the large-eddy time scale associated with the overturning of large eddies in the system. For $Fr_k > 1$, the large eddies overturn faster than the time needed for reversible exchange between k_w and k_p , allowing irreversible mixing associated with eddy turnover. For $Fr_k \sim \mathcal{O}(1)$, the large eddies overturn at a comparable rate needed for reversible exchange between k_w and k_p . Finally, for $Fr_k < 1$, the large eddies overturn

Quantity	Quadrant 1	Quadrant 2	Quadrant 3	Quadrant 4
Vertical density flux ($w\rho$)	$w > 0, \rho > 0$ ($w\rho > 0$, converts k_w to k_p): positive vertical velocity fluctuation with positive density anomaly	$w < 0, \rho > 0$ ($w\rho < 0$, converts k_p to k_w): negative vertical velocity fluctuation with positive density anomaly	$w < 0, \rho < 0$ ($w\rho > 0$, converts k_w to k_p): negative vertical velocity fluctuation with negative density anomaly	$w > 0, \rho < 0$ ($w\rho < 0$, converts k_p to k_w): positive vertical velocity fluctuation with negative density anomaly
Nonlinear pressure–strain ($p_{NL}\partial_z w$)	$p_{NL} > 0, \partial_z w > 0$ ($p_{NL}\partial_z w > 0$, converts k_H to k_w): strain-dominated regions with vertical divergence	$p_{NL} < 0, \partial_z w > 0$ ($p_{NL}\partial_z w < 0$, converts k_w to k_H): rotation-dominated regions with vertical divergence	$p_{NL} < 0, \partial_z w < 0$ ($p_{NL}\partial_z w > 0$, converts k_H to k_w): rotation-dominated regions with vertical convergence	$p_{NL} > 0, \partial_z w < 0$ ($p_{NL}\partial_z w < 0$, converts k_w to k_H): strain-dominated regions with vertical convergence
Buoyancy pressure–strain ($p_B\partial_z w$)	$p_B > 0, \partial_z w > 0$ ($p_B\partial_z w > 0$, converts k_H to k_w): unstable density gradients with vertical divergence	$p_B < 0, \partial_z w > 0$ ($p_B\partial_z w < 0$, converts k_w to k_H): stable density gradients with vertical divergence	$p_B < 0, \partial_z w < 0$ ($p_B\partial_z w > 0$, converts k_H to k_w): stable density gradients with vertical convergence	$p_B > 0, \partial_z w < 0$ ($p_B\partial_z w < 0$, converts k_w to k_H): unstable density gradients with vertical convergence
Nonlinear pressure scrambling ($p_{NL}\partial_z \rho$)	$p_{NL} > 0, \partial_z \rho > 0$ ($p_{NL}\partial_z \rho > 0$, generates B): strain-dominated regions with unstable density gradients	$p_{NL} < 0, \partial_z \rho > 0$ ($p_{NL}\partial_z \rho < 0$, destroys B): rotation-dominated regions with unstable density gradients	$p_{NL} < 0, \partial_z \rho < 0$ ($p_{NL}\partial_z \rho > 0$, generates B): rotation-dominated regions with stable density gradients	$p_{NL} > 0, \partial_z \rho < 0$ ($p_{NL}\partial_z \rho < 0$, destroys B): strain-dominated regions with stable density gradients
Buoyancy pressure scrambling ($p_B\partial_z \rho$)	$p_B > 0, \partial_z \rho > 0$ ($p_B\partial_z \rho > 0$, generates B): unstable density gradients with unstable density gradients	$p_B < 0, \partial_z \rho > 0$ ($p_B\partial_z \rho < 0$, destroys B): stable density gradients with unstable density gradients	$p_B < 0, \partial_z \rho < 0$ ($p_B\partial_z \rho > 0$, generates B): stable density gradients with stable density gradients	$p_B > 0, \partial_z \rho < 0$ ($p_B\partial_z \rho < 0$, destroys B): unstable density gradients with stable density gradients

Table 2. Descriptions of the contributions from the four quadrants to the five correlations of interest: (i) vertical density flux, (ii) nonlinear pressure–strain term, (iii) buoyancy pressure–strain term, (iv) nonlinear pressure scrambling term and (v) buoyancy pressure scrambling term.

more slowly than the reversible exchange between k_w and k_p , allowing parcels to return to their equilibrium position before they can fully mix.

If we recall that Rotta-style return-to-isotropy models take τ_L as the time scale associated with the pressure–strain redistribution, we can also interpret the turbulent Froude number as a measure of the relative importance of two reversible exchange processes: (i) reversible exchange between k_H and k_w by pressure–strain redistribution occurring over τ_L ; (ii) reversible exchange between k_w and k_p by vertical buoyancy flux occurring over τ_B . For $Fr_k > 1$, reversible exchange between k_H and k_w occurs more rapidly and thus more effectively than the reversible exchange between k_w and k_p . However, there is negligible overall mixing of density because the background density gradient is negligible, and the turbulence is weakly anisotropic, resulting in negligible pressure–strain redistribution. For $Fr_k \sim \mathcal{O}(1)$, reversible exchange between k_H and k_w by pressure–strain redistribution, and reversible exchange between k_w and k_p by vertical buoyancy flux occur at comparable rates. The background density gradient is significant and damps k_w relative to k_H , which results in large-scale anisotropy, but pressure–strain redistribution occurs rapidly enough to sustain k_w , which in turn generates vertical

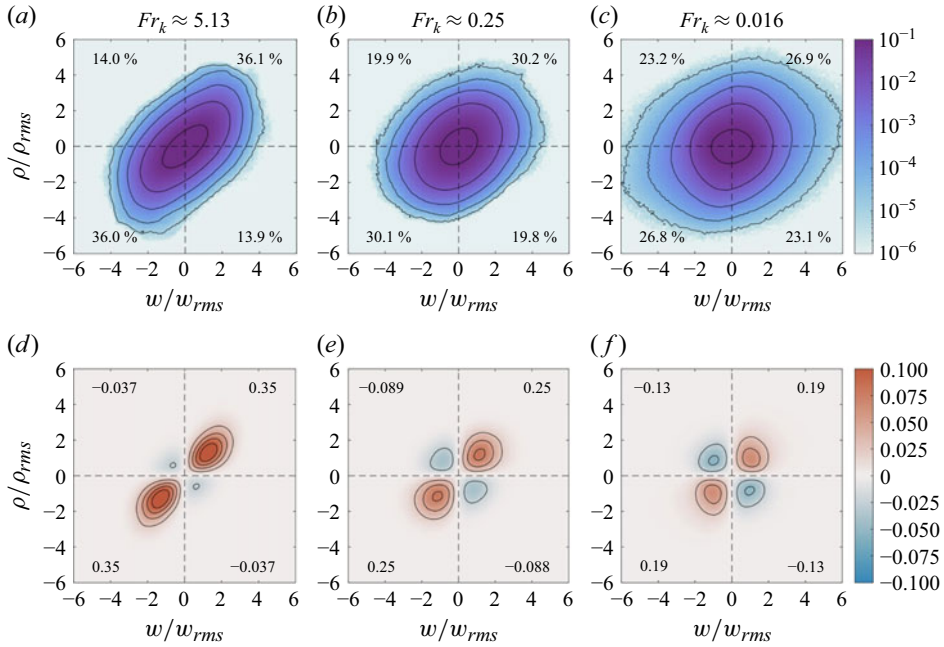


Figure 7. (a–c) Joint probability distribution functions (p.d.f.s) and (d–f) covariance integrands of the normalised vertical density flux ($w\rho/(w_{rms}\rho_{rms})$) for (a,d) very weak, (b,e) strong and (c,f) very strong stability. For panels (a–c), the text in each quadrant indicates the probability within each quadrant, whereas for panels (d–f), the text in each quadrant indicates that quadrant’s contribution towards the overall correlation.

buoyancy flux and sustains the reversible exchange between k_w and k_p (see [figures 5b](#) and [5d](#)). For $Fr_k < 1$, the reversible exchange of k_H and k_w occurs more slowly than the reversible exchange between k_w and k_p by vertical buoyancy flux. This results in a reduced generation of k_w by pressure–strain redistribution, which decreases B because of a reduction in its primary generation mechanism (i.e. source due to k_w , $2N^2k_w$; see [figure 5d](#)). This then limits the conversion of k_w to k_p , preventing the complete decay of vertical perturbations.

Next, we quantify the contributions of the down-gradient and counter-gradient flux events to the overall flux by plotting the covariance integrand associated with these two joint p.d.f.s in [figure 7\(d,e,f\)](#). For each bin, the covariance integrand is computed by taking the values of the two variables and the associated value of the joint p.d.f., and multiplying them together. It thus represents the contribution of each bin to the overall flux. Down-gradient fluxes are shown in red and counter-gradient fluxes are shown in blue. As stability increases (left to right), we note that the down-gradient fluxes become less positively correlated, whereas the counter-gradient fluxes become more negatively correlated, resulting in a weaker positive correlation of the overall flux with increasing stability. Since both variables (w and ρ) are normalised by their root-mean-squared values, summing across the four quadrants results in the correlation coefficient rather than the overall flux, which is important to keep in mind to avoid incorrectly concluding that the buoyancy flux is stronger for the weakest stability simulation than for the strongest stability simulation. The correlation coefficient can be interpreted as a transport efficiency (Li & Bou-Zeid 2011). Therefore, this result indicates that the vertical density flux is more effective (positively correlated) for weaker stability than for stronger stability, but we note from [figure 5\(b\)](#) that the buoyancy flux is negligible for the weakest stability case

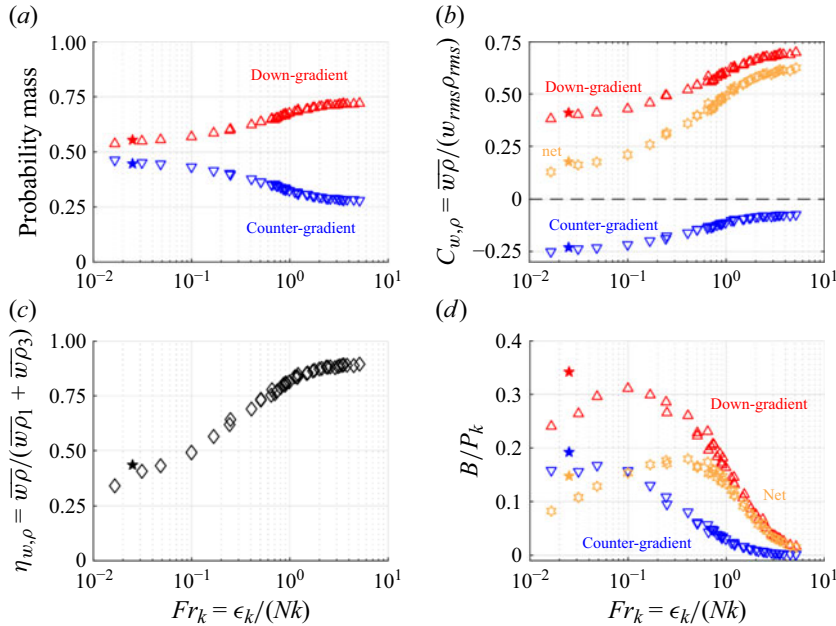


Figure 8. (a) Probability mass of down-gradient and counter-gradient events (red and blue triangles, respectively), (b) correlation of down-gradient and counter-gradient events and the overall flux (orange triangles), (c) efficiency of the vertical density flux, and (d) normalised vertical buoyancy flux associated with the down-gradient, counter-gradient and overall flux as a function of Fr_k . The efficiency is defined as the net flux (sum over all quadrants) divided by the sum over just the down-gradient fluxes (sum over only quadrants 1 and 3). The orange stars are the net vertical buoyancy flux, and P_k is the rate of production of TKE. The results from the higher Reynolds number simulation (V2_128) are denoted by filled stars.

($Fr_k \approx 5.13$), exhibits its peak value for the strong stability case ($Fr_k \approx 0.25$) and weakens but remains finite for the strongest stability case ($Fr_k \approx 0.016$).

To further understand how the contributions from the down-gradient and counter-gradient fluxes vary with increasing stability, we plot the following quantities as a function of Fr_k in figure 8: (a) the probability mass of down-gradient (red triangles) and counter-gradient events (blue triangles); (b) the correlation of down-gradient and counter-gradient events (blue triangles) and the correlation of the overall flux (orange stars); (c) the efficiency of the vertical buoyancy flux defined as the net vertical density flux normalised by the sum of only the down-gradient contributions; (d) the normalised buoyancy flux magnitudes associated with the down-gradient and counter-gradient events and the overall flux. We have chosen to combine the down-gradient and counter-gradient quadrants together to simplify our plots since the probability mass and correlations for the individual down-gradient and counter-gradient quadrants were quite similar to one another for all stability values, as expected given that our simulation set-up is homogeneous in the vertical direction, and invariant to vertical reflection of the density gradient and gravity force.

In figure 8(a), we see that for weak stratification, down-gradient fluxes occur approximately 75 % of the time and counter-gradient fluxes occur approximately 25 % of the time, and as stability is increased, we see that counter-gradient fluxes occur more frequently, such that the down-gradient and counter-gradient fluxes approach equal likelihoods. In figure 8(b), we plot the correlation coefficient associated with the down-gradient, counter-gradient and overall flux (red and blue triangles and orange stars) as a function of Fr_k . For weak stability, the down-gradient fluxes are strongly correlated

with a value near 0.75, and the overall flux has a slightly weaker correlation due to the weak but finite negative correlations associated with the counter-gradient fluxes. With increasing stability, the down-gradient fluxes become more weakly correlated, whereas the counter-gradient fluxes become more strongly correlated, which drives the correlation of the overall flux towards zero and indicates less effective vertical density exchange. In [figure 8\(c\)](#), we plot another measure of the efficiency of the vertical density flux defined as the net flux normalised by the contributions from just the down-gradient fluxes. We note that for weak stability, the efficiency of the vertical density flux is approximately 0.9, but it monotonically weakens with increasing stability due to increasing contributions from counter-gradient fluxes. Lastly, in [figure 8\(d\)](#), we plot the normalised vertical buoyancy flux magnitudes associated with the down-gradient, counter-gradient and overall fluxes (red and blue triangles and orange stars). Because the turbulence is statistically stationary and triply homogeneous, we note that the orange symbols are equivalent to the mixing coefficient Γ . When the stratification is weak relative to turbulence ($Fr_k > 1$), we note that increasing the background stratification results in sharp increases in the down-gradient fluxes, which are not accompanied by similar increases in the counter-gradient fluxes. As stratification and turbulence both become important ($Fr_k \sim \mathcal{O}(1)$), increasing the background stratification results in further enhancement of the down-gradient fluxes, but now this is accompanied by increases in the counter-gradient fluxes as well. This indicates simultaneous exchanges between k_w and k_p in both directions (i.e. conversion of k_w into k_p and conversion of k_p into k_w) that are comparable in magnitude but with a net sum that still results in a net conversion of k_w into k_p . Lastly, when stratification becomes very strong ($Fr_k < 0.1$), increasing the background stratification results in a weakening of the down-gradient fluxes (red triangles), but the contributions from the counter-gradient fluxes remain largely unchanged (blue triangles), which indicates that the transfer from k_w to k_p becomes weaker, but the transfer from k_p to k_w remains largely unchanged.

Regarding the greater buoyancy flux magnitudes observed for the higher Reynolds number simulation (V2_128) ($Fr_k \approx 0.025$), we note that the correlations and the efficiency values reported in [figures 8\(b\)](#) and [8\(c\)](#) are similar for this case to those for the lower Reynolds simulation ($Fr_k \approx 0.31$), which indicates that this change must be driven by the enhanced pressure–strain redistribution of k_H to k_w in the higher Reynolds number simulation (see [figure 5b](#)). We also note that while approaching the limit of $Fr_k \ll 1$ might lead to down-gradient and counter-gradient contributions becoming increasingly similar, resulting in a net zero flux, the turbulent flow would still involve exchanges among the horizontal, vertical and potential energy components, a net downscale cascade of energy, and dissipation at the viscous and diffusive scales. This is physically very different from the canonical set-up of adiabatically displacing fluid parcels in a stably stratified fluid that is initially at rest, which also involves a net zero buoyancy flux (no net exchange between k_w and k_p) due to exact compensation between down-gradient and counter-gradient fluxes, but which lacks other physical aspects that are present for three-dimensional, stably stratified, turbulent flows (e.g. net downscale energy cascade and dissipative losses).

Next, we seek to further understand how the contributions from the four quadrants of the pressure–strain correlations contribute to the overall redistribution of k_H into k_w by plotting the following quantities as a function of Fr_k in [figure 9](#): (panels *a,b,c*) probability mass of the four quadrants of the pressure–strain correlations (Q1, red triangles; Q2, orange triangles; Q3, blue squares; Q4, purple circles); (panels *d,e,f*) correlations of the events that redistribute k_H into k_w (red triangles), events that redistribute k_w into k_H (blue triangles) and overall pressure–strain redistribution (black exes); (panels *g,h,i*) efficiency of the pressure–strain correlation; (panels *j,k,l*) normalised pressure–strain correlations associated with conversion of k_H into k_w , conversion of k_w into k_H , and the overall

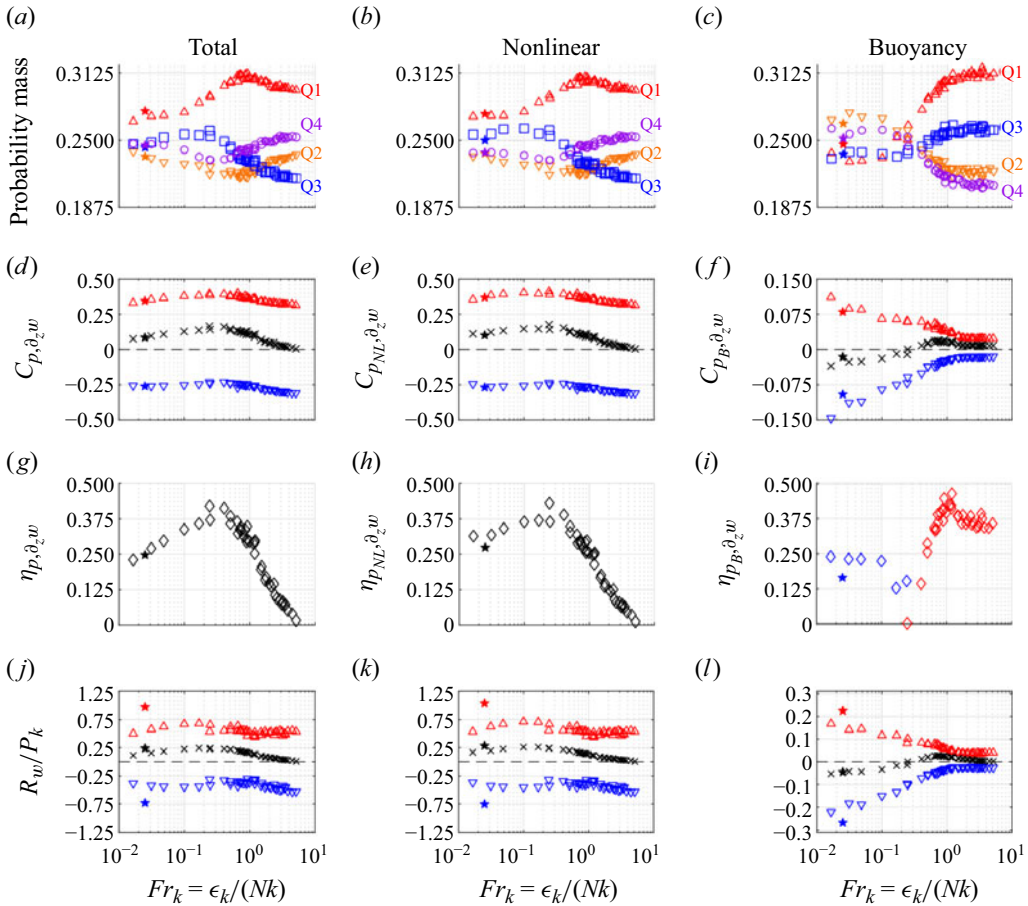


Figure 9. (a–c) Probability mass of the four quadrants of the pressure–strain correlations (Q1, red triangles; Q2, orange triangles; Q3, blue squares; Q4, purple circles); (d–f) correlation of the events that redistribute k_H into k_w (red triangles), events that redistribute k_w into k_H (blue triangles) and overall pressure–strain redistribution (black exes); (g–i) efficiency of the pressure–strain correlation; (j–l) normalised pressure–strain correlations associated with conversion of k_H into k_w , conversion of k_w into k_H and the overall redistribution (same symbols/colors convention as panels d–f). All variables are plotted as a function of Fr_k . The results from the higher Reynolds number simulation (V2_128) are denoted by filled stars.

redistribution. The associated contour plots of the joint p.d.f.s and covariance integrands are shown in figures 13 and 14 in Appendix B.

We note that the peak pressure–strain correlation value is reached at $Fr_k \approx 0.3$ (panel d), which coincides with the maximum probability mass values associated with Q3 redistribution events (k_H into k_w ; blue squares in figure 9a) and minimum values associated with Q2 and Q4 redistribution events (k_w into k_H ; orange triangles and purple circles in figure 9a). This also coincides with the maximum efficiency of the overall pressure–strain correlation, shown by the peak in $\eta_{p, \partial_z w}$ defined as the net pressure–strain correlation normalised by the sum over just the Q1 and Q3 redistribution events, which convert k_H into k_w (panel g). Focusing just on the nonlinear component of the pressure–strain correlations, we note that the peak correlation persists until stronger stability ($Fr_k \approx 0.1$) (panel e), and associatedly, the efficiency of the nonlinear pressure–strain correlation and normalised net redistribution (R_w / P_k) both exhibit weaker declines

for $Fr_k < 0.1$ compared with the total pressure–strain correlation (compare panels h and k with panels g and j). These differences can be explained by considering the buoyancy component of the pressure–strain correlations (panels f, i, l). At weak stratification, Q1 and Q3 redistribution events (conversion of k_H into k_w) dominate over Q2 and Q4 redistribution events (conversion of k_w into k_H) (panel c), but the overall correlation (panel f) and normalised redistribution (panel l) are negligible due to the buoyancy effects being weak. As stratification increases until $Fr_k \approx 0.7$, we note that the probability masses of the four quadrants change insignificantly, but with stronger buoyancy effects, the correlation and normalised redistribution values now begin to contribute meaningfully to the overall redistribution, where, on average, the buoyancy pressure–strain correlation converts k_H into k_w . With further increasing stratification, the probability masses of the Q1 and Q3 redistribution events decrease, while the probability masses of the Q2 and Q4 redistribution events increase. This is related to a strengthening negative correlation associated with the events that convert k_w into k_H (blue triangles; panel f), which drives the overall correlation to change signs and become increasingly negative (black exes). Because the overall term changes sign, we compute the efficiency of the buoyancy pressure–strain correlation in two ways, where the positive values of the overall buoyancy pressure–strain component are normalised by the sum of the Q1 and Q3 events (red diamonds), and the negative values of the overall buoyancy pressure–strain component are normalised by the sum of the Q2 and Q4 events (blue diamonds). The peak efficiency of ~ 0.4 associated with redistribution from k_H into k_w occurs at $Fr_k \approx 1$, whereas the peak efficiency hovers at approximately 0.25 for redistribution from k_w into k_H for $Fr_k < 0.1$. Before moving on, we reiterate that unlike the prevailing description of the nonlinear pressure–strain correlation as promoting large-scale isotropy, which is associated with a definite sign for the term, the buoyancy pressure–strain correlation exhibits more complex behaviour that promotes large-scale isotropy for weak to moderate stability, but then begins to promote large-scale anisotropy for stronger stability. Given that its overall effect is sensitive to the strength of the background stratification, this hints at similarities with and connections to the vertical buoyancy flux, which comprises both significant down-gradient fluxes, converting k_w into k_p , and counter-gradient fluxes, converting k_p into k_w . In §4.4, we will mathematically demonstrate the link between the buoyancy pressure–strain redistribution and vertical buoyancy flux and explain this sign-change behaviour associated with increasing stability.

Now, we seek to understand how the contributions from the four quadrants of the pressure scrambling correlations contribute to the generation or destruction of the vertical buoyancy flux. In figure 10, we plot the following quantities as a function of Fr_k : (panels a, b, c) probability mass of the four quadrants of the pressure scrambling correlations (Q1, red triangles; Q2, orange triangles; Q3, blue squares; Q4, purple circles); (panels d, e, f) correlations of the events that generate B (red triangles), events that destroy B (blue triangles) and overall pressure scrambling correlation (black exes); (panels g, h, i) efficiency of the pressure scrambling correlation; (panels j, k, l) normalised pressure scrambling correlations associated with generation of B (red), destruction of B (blue) and the net effect (black). The associated contour plots of the joint p.d.f.s and covariance integrands are shown in figures 15 and 16 in Appendix B.

Recall that the net pressure scrambling term changes signs at $Fr_k \approx 0.1$ as stability increases from near neutral conditions (cf. figure 10j). This is associated with relatively small changes in the probability mass associated with Q1 and Q2 events but decreasing mass associated with Q4 events (destruction of B) and increasing mass associated with Q3 events (generation of B). These changes are broadly reflected also in the nonlinear and buoyancy components as well (see figure 10b,c). Connectedly, the overall correlation of

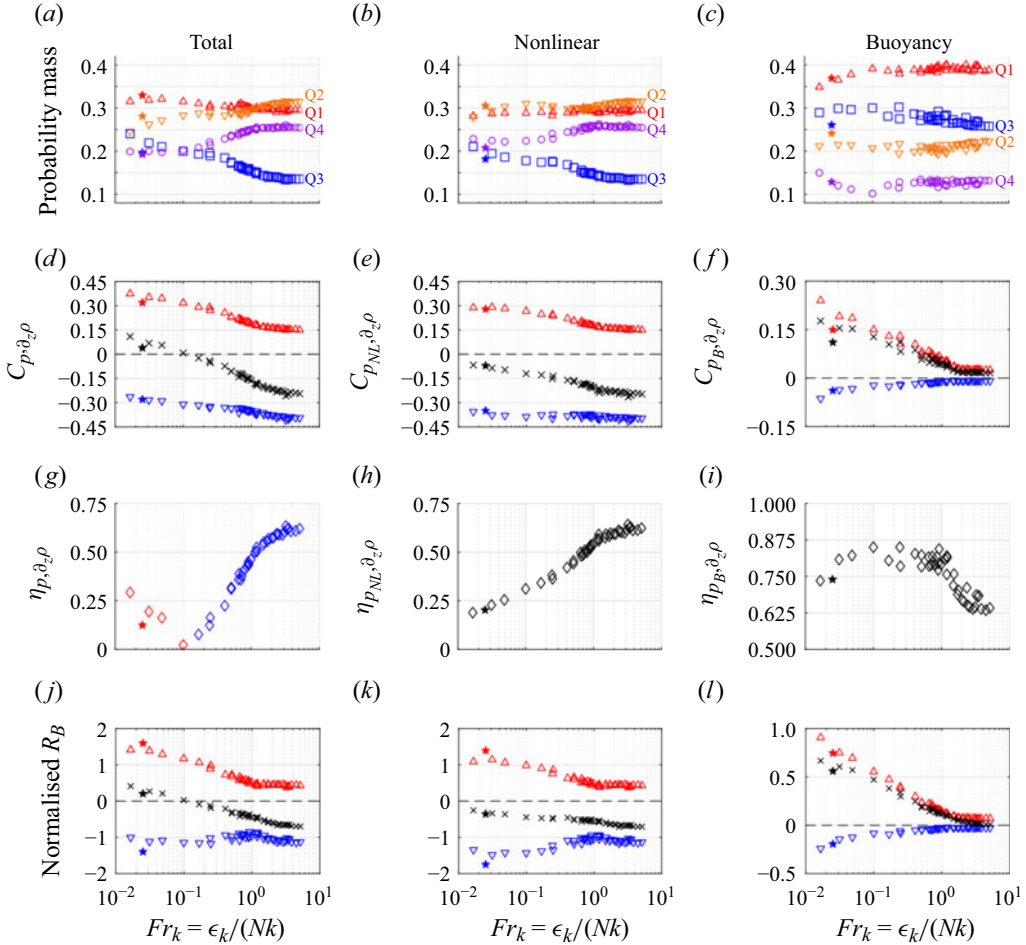


Figure 10. (a–c) Probability mass of the four quadrants of the pressure scrambling correlations (Q1, red triangles; Q2, orange triangles; Q3, blue squares; Q4, purple circles); (d–f) correlation of the events that generate buoyancy flux B (red triangles), events that destroy buoyancy flux (blue triangles) and overall pressure scrambling term (black exes); (g–i) efficiency of the pressure scrambling term; (j–l) normalised pressure scrambling term associated with generation of B , destruction of B , net effect on $d_t B$ (same symbols/colours convention as panels d–f). All variables are plotted as a function of Fr_k . The results from the higher Reynolds number simulation (V2_128) are denoted by filled stars.

the pressure scrambling term (black exes in figure 10d) also switches signs at $Fr_k \approx 0.1$, and this is due to both an increasing positive correlation of the sum of Q1 and Q3 events, which generate vertical buoyancy flux, and a reduced correlation of the sum of Q2 and Q4 events, which destroy vertical buoyancy flux. Looking at the correlation of the nonlinear component of pressure scrambling (panel e), we note that it is always negatively correlated, but this weakens due to an increasing contribution from positively correlated, nonlinear pressure scrambling events. The correlation of the buoyancy component of pressure scrambling is always positive (panel f), and the negatively correlated buoyancy pressure scrambling events remain negligible until $Fr_k < 0.1$.

Next, we consider the efficiencies associated with the three pressure scrambling correlations (panels g, h, i). For the total pressure scrambling term (figure 10g), we define the efficiency by normalising the net pressure scrambling correlation by the sum of Q2 and Q4 events when the correlation is negative (blue diamonds), and by the sum of Q1 and Q3

events when the correlation is positive (red diamonds). The overall pressure scrambling is most efficient at neutral stability with an efficiency slightly above 60 %, but after the sign-change at $Fr_k \approx 0.1$, the efficiency generally increases with stability. For the nonlinear pressure scrambling term (figure 10h), we note that the efficiency is largest for weak stratification, and monotonically decreases with increasing stability. For the buoyancy pressure scrambling term (figure 10i), the efficiency increases with stability and reaches a maximum value of approximately 80 % before decreasing for $Fr_k < 0.1$. In closing, we stress that the overall buoyancy pressure scrambling term is sign definite with negligible contributions from the negatively correlated contributions until stability becomes strong ($Fr_k < 0.1$). We will seek to mathematically understand this behaviour in the next section.

4.4. Analytical expressions for the buoyancy component of pressure correlations and further physical interpretation

In this section, we seek to mathematically explain two particular observations about the buoyancy pressure correlations. First, as shown in figure 6(b), the buoyancy component of the pressure–strain correlation changes sign at strong stability and begins to redistribute k_w into k_H . This behaviour is in contrast to the physical picture underlying the Rotta-type, return-to-isotropy models that are often used to close the Reynolds stress equations (though non-Rotta models have been proposed for the buoyancy-linked redistribution; e.g. Hanjalić & Launder 2022). Second, the buoyancy component of the pressure scrambling seems sign definite (see figure 6c), and it generally increases monotonically with stratification. This behaviour contrasts with the classic view of pressure scrambling terms as a sink of passive scalar fluxes, which decorrelate the velocity and scalar fields.

To explain these effects, we return to (4.3) and consider the Fourier coefficients of the buoyancy component of the pressure fluctuations,

$$\hat{p}_B(\boldsymbol{\kappa}, t) = \frac{ig\kappa_z\hat{\rho}(\boldsymbol{\kappa}, t)}{\kappa^2}, \quad (4.8)$$

where $i = \sqrt{-1}$ is the imaginary unit and $\hat{\rho}(\boldsymbol{\kappa}, t)$ are the Fourier coefficients associated with the density field. Next, we define $g_1(\mathbf{x}, t) = (1/\rho_0)p_B\partial_z w$ and $g_2(\mathbf{x}, t) = (g/\rho_0^2)p_B\partial_z\rho$, which are the unaveraged buoyancy components of the pressure–strain and pressure scrambling terms, respectively. Taking the forward Fourier transform of g_1 and g_2 in the three spatial dimensions and applying the Dirac delta function (cf. Appendix D of Pope 2000) to collapse one of the integrals, we arrive at the following expressions:

$$\hat{g}_1(\boldsymbol{\kappa}, t) = \frac{g}{\rho_0} \int d\boldsymbol{\kappa}' \left[-\frac{\kappa'_z(\kappa_z - \kappa'_z)}{\kappa'^2} \right] \hat{\rho}(\boldsymbol{\kappa}', t) \hat{w}(\boldsymbol{\kappa} - \boldsymbol{\kappa}', t), \quad (4.9)$$

$$\hat{g}_2(\boldsymbol{\kappa}, t) = \left(\frac{g}{\rho_0} \right)^2 \int d\boldsymbol{\kappa}' \left[-\frac{\kappa'_z(\kappa_z - \kappa'_z)}{\kappa'^2} \right] \hat{\rho}(\boldsymbol{\kappa}', t) \hat{\rho}(\boldsymbol{\kappa} - \boldsymbol{\kappa}', t), \quad (4.10)$$

where $\hat{w}(\boldsymbol{\kappa}, t)$ are the Fourier coefficients associated with the vertical velocity field. This derivation involves similar steps as in § 6.4.2 of Pope (2000), where the nonlinear advection term of the Navier–Stokes equations is expressed in Fourier space. Because we are interested in the volume-averaged effect of the buoyancy components of the pressure–strain and pressure scrambling terms, we set $\boldsymbol{\kappa} = 0$ in (4.9) and (4.10) and find

$$R_{w,B} = \hat{g}_1(\boldsymbol{\kappa} = 0, t) = \frac{g}{\rho_0} \int d\boldsymbol{\kappa}' \left(\frac{\kappa'_z}{\kappa'} \right)^2 \hat{\rho}(\boldsymbol{\kappa}', t) \hat{w}^*(\boldsymbol{\kappa}', t), \quad (4.11)$$

$$R_{B,B} = \hat{g}_2(\boldsymbol{\kappa} = 0, t) = \left(\frac{g}{\rho_0} \right)^2 \int d\boldsymbol{\kappa}' \left(\frac{\kappa'_z}{\kappa'} \right)^2 \hat{\rho}(\boldsymbol{\kappa}', t) \hat{\rho}^*(\boldsymbol{\kappa}', t), \quad (4.12)$$

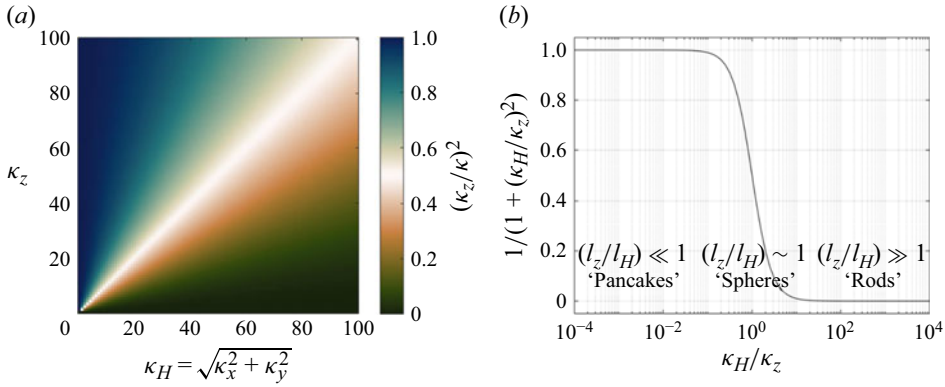


Figure 11. Weighting factor $(\kappa_z/\kappa)^2 = 1/[1 + (\kappa_H/\kappa_z)^2]$ in (4.11) and (4.12) plotted as a function of (a) the horizontal and vertical wavenumbers (κ_H and κ_z) and (b) an aspect ratio based on the horizontal and vertical wavenumbers (κ_H/κ_z).

where we have used the conjugate symmetry of Fourier coefficients of real functions to rewrite $\hat{w}(-\kappa', t) = \hat{w}^*(\kappa', t)$ and $\hat{\rho}(-\kappa', t) = \hat{\rho}^*(\kappa', t)$.

There are several key aspects of (4.11) and (4.12). First, the volume-averaged buoyancy component of the pressure–strain correlation ($R_{w,B}$) (4.11) involves a weighted integral of the buoyancy flux cospectrum, where positive values of the integrand are associated with down-gradient vertical buoyancy fluxes, and negative values of the integrand are associated with counter-gradient vertical buoyancy fluxes. This reveals that down-gradient vertical buoyancy fluxes are connected to redistribution of k_H into k_w and that counter-gradient vertical buoyancy fluxes are connected to redistribution of k_w into k_H . Second, the volume-averaged buoyancy component of the pressure scrambling term ($R_{B,B}$) involves a weighted integral of the density variance spectrum (related to TPE). The integrand is quadratic, implying that the term is positive semidefinite (zero in the neutral limit). Note that without the wavenumber-dependent weighting factors, the integrals in (4.11) and (4.12) would be related to $\overline{w\rho}$ and $\overline{\rho\rho}$. Third, the weighting factor $(\kappa_z/\kappa)^2$, which appears in both expressions, more strongly weights contributions from pancake structures ($\kappa_z \gg \kappa_H$, where $\kappa^2 = \kappa_x^2 + \kappa_y^2 + \kappa_z^2 = \kappa_H^2 + \kappa_z^2$ with $\kappa_H = \sqrt{\kappa_x^2 + \kappa_y^2}$), which are prominent dynamical features of stratified turbulent flows (e.g. Lin & Pao 1979; Hopfinger 1987; Riley & Lelong 2000; Billant & Chomaz 2001; Lindborg 2006; Shah & Bou-Zeid 2014; Caulfield 2021; Kimura & Sullivan 2024). To aid this interpretation, we plot the weighting factor $(\kappa_z/\kappa)^2$ as a function of κ_H and κ_z in figure 11(a) and also as a function of an aspect ratio κ_H/κ_z in figure 11(b) (or also l_z/l_H , where l_H and l_z are the horizontal and vertical length scales associated with the horizontal and vertical wavenumbers, $\kappa_H = 2\pi/l_H$ and $\kappa_z = 2\pi/l_z$). This latter plot uses a re-expressed statement of the weighting factor where the numerator and denominator have been divided through by κ_z^2 . In both plots, the weighting factor approaches unity when $\kappa_z \gg \kappa_H$ (or equivalently, $l_z/l_H \ll 1$). The weighting factors in (4.11) and (4.12) reveal that the effect of stratification manifests in an anisotropic manner in Fourier space, which would be missed when only accounting for the wavenumber magnitude. Lastly, we note that (4.11) and (4.12) apply generally to all homogeneous stratified flows independent of forcing (e.g. decaying, forced, sheared, etc.) and across all stability conditions (neutral, stable, unstable). This fact

helps explain why some relationships between R_w , R_B and Γ have been observed across different types of stratified turbulent flows (e.g. Yi & Koseff 2022a, 2023).

With these points in mind, we return to figures 6(b) and 6(c) to interpret the buoyancy components of the pressure–strain and pressure scrambling terms. First, the buoyancy component of the pressure–strain correlation begins to decrease at $Fr_k \approx 0.7$ and becomes increasingly negative for $Fr_k < 0.3$ (see figure 6b). Since the volume-averaged buoyancy flux remains positive for all values of Fr_k (i.e. $\overline{w\rho} > 0$), we note from (4.11) that $R_{w,B} < 0$ must result from stronger counter-gradient buoyancy fluxes associated with layered structures that become more favourably weighted after the multiplication by $(\kappa_z/\kappa)^2$. This means that, on average, counter-gradient buoyancy fluxes associated with layered motions contribute to redistribution of k_w into k_H , opposing large-scale return-to-isotropy. Relatedly, we observed more frequent and stronger contributions from counter-gradient fluxes in figure 8 with increasing stability. Because $R_{w,B} < 0$ for $Fr_k < 0.3$ is the result of volume and time averaging, this implies that there are persistent, large-scale, counter-gradient buoyancy fluxes, a result that was also observed by Almalkie & de Bruyn Kops (2012) for forced, homogeneous, stably stratified turbulence, and by Kaltenbach, Gerz & Schumann (1994) for stably stratified, homogeneous shear turbulence simulations for $Ri_g = 0.5$ and $Pr = 1$. In the literature, these features have been treated distinctly from persistent, counter-gradient buoyancy fluxes at small scales (e.g. Holt, Koseff & Ferziger 1992; Kaltenbach *et al.* 1994; Gerz & Schumann 1996). Second, the buoyancy component of the pressure scrambling term is positive semidefinite and increases monotonically with stratification (see figure 6c). From (4.12), we see that this is due to the integrand of $R_{B,B}$ being quadratic and vanishing in the limit of neutral stability.

5. Conclusions

In this work, we studied how two specific pressure correlations (i.e. vertical pressure–strain redistribution and vertical pressure scrambling) changed as a function of increasing stability, using a DNS dataset of linearly forced, stably stratified turbulence from Yi & Koseff (2022a). The vertical pressure–strain redistribution term appears in the k_w budget (3.7), and we highlighted its key role in setting the magnitude of the mixing efficiency (and therefore Γ) in § 2. Also, the vertical pressure scrambling term appears in the vertical buoyancy flux (B) budget (3.8), and while the term acts as a significant sink of B for neutral and weak stability, it changes sign and begins to correlate w and ρ , generating vertical buoyancy flux for strong stability.

To further analyse these two pressure correlations, we decomposed the pressure field into nonlinear and buoyancy components and studied them separately as a function of increasing stability. First, we observed that the rise, and plateau, of Γ going from neutral to strong stability (figure 5c) is primarily connected to an increase in the nonlinear pressure–strain redistribution that enhances the exchange of k_H into k_w (figure 6b). The subsequent decline of Γ going from strong to very strong stability (figure 5c) is due to both a weakening of the nonlinear pressure–strain redistribution (reducing the exchange of k_H into k_w) and a sign change and strengthening of the buoyancy pressure–strain redistribution (enhancing the exchange of k_w into k_H) (figure 6b). Relatedly, these changes are connected with (i) a reduction in the primary generation mechanism of B (i.e. source due to k_w , $2N^2k_w$; see figure 5d), and (ii) the associated change in the sign of the pressure scrambling term needed to ensure that B remains positive, which is expected for stably stratified flows. We found that this sign change is due to a compensation between the nonlinear and buoyancy components of pressure scrambling. Furthermore, the buoyancy pressure scrambling continues to increase in magnitude for very strong stability, while the

nonlinear pressure scrambling continues to decrease in magnitude such that the overall term becomes an increasingly important means of generating B (see figure 6c).

To better understand these pressure correlations, we first arrived at a set of physical interpretations for the nonlinear and buoyancy pressure fluctuations, where positive and negative nonlinear pressure fluctuations are connected to strain-dominated and rotation-dominated regions, respectively, and positive and negative buoyancy pressure fluctuations are connected to regions with unstable and stable density gradients, respectively. Then, we conducted quadrant analyses of the vertical buoyancy flux and the nonlinear and buoyancy components of the pressure–strain correlation and pressure scrambling terms (see table 2) to quantify how the four different contributions summed together to bring about the overall volume-averaged values of these five correlations.

For the buoyancy pressure correlations in particular, we showed mathematically that the volume-averaged buoyancy pressure–strain component is given by a weighted integral of the cospectrum of the vertical buoyancy flux (4.11), such that down-gradient buoyancy fluxes contribute to the conversion of k_H into k_w and counter-gradient buoyancy fluxes contribute to the conversion of k_w into k_H . This highlights a key physical concept that the presence of stable stratification not only modifies the exchange between k_w and k_p , but also fundamentally alters the exchange between k_H and k_w . In addition, we showed mathematically that the volume-averaged buoyancy pressure scrambling is given by a weighted integral of the spectrum of the density variance (4.12), revealing that this term is positive semidefinite. The weighting factor of $(\kappa_z/\kappa)^2$ indicates stronger contributions from layered/pancake structures ($\kappa_z \gg \kappa_H$), which are important dynamical features of strongly stratified turbulence. Furthermore, these expressions apply generally to all homogeneous stratified flows independent of forcing (e.g. decaying, forced, sheared, etc.) and across all stability conditions (neutral, stable, unstable), which helps to explain why these effects have been observed for both forced and sheared stably stratified turbulence simulations (e.g. Shah & Bou-Zeid 2014; Yi & Koseff 2022a, 2023).

One avenue for future work is to study how the various generation and exchange processes associated with k_H , k_w and B behave in time-evolving flows (e.g. Riley & de Bruyn Kops 2003; Hebert & de Bruyn Kops 2006; de Bruyn Kops & Riley 2019) and wall-bounded flows (e.g. Heinze, Mironov & Raasch 2016; Pearson, Grant & Polton 2019) given the prominent impact of wall-blockage and shear on pressure–strain and pressure scrambling dynamics, and the importance of such flows in various geophysical applications. Another interesting avenue for future work is to study the interplay of intercomponent exchange and downscale transfer for stably stratified turbulence (e.g. Johnson 2020, 2021; Zhang *et al.* 2022; Bragg & de Bruyn Kops 2024a) and to incorporate information about scalewise anisotropy as a function of wavenumber magnitude into cospectral models that are commonly used in large-scale models of the Earth and climate systems (e.g. Ayet *et al.* 2020). Finally, building on the comparison between simulations at two different Reynolds numbers at strong stability (e.g. figure 5), a more comprehensive exploration of the multiparameter dependence of Γ as discussed in § 2 is necessary for a more holistic understanding of how energy exchange and buoyancy flux generation in stratified turbulent flows depends on both the ranges of anisotropic and isotropic scales of motion.

Acknowledgements. The statements, findings, conclusions, and recommendations are those of the authors and do not necessarily reflect the views of the National Oceanic and Atmospheric Administration, or the U.S. Department of Commerce.

Funding. Y.R.Y. gratefully acknowledges support from the Charles H. Leavell Fellowship of the Department of Civil and Environmental Engineering at Stanford University, the Stanford Woods Institute for the Environment, and the Postdoctoral Environmental Teaching Fellowship from the High Meadows

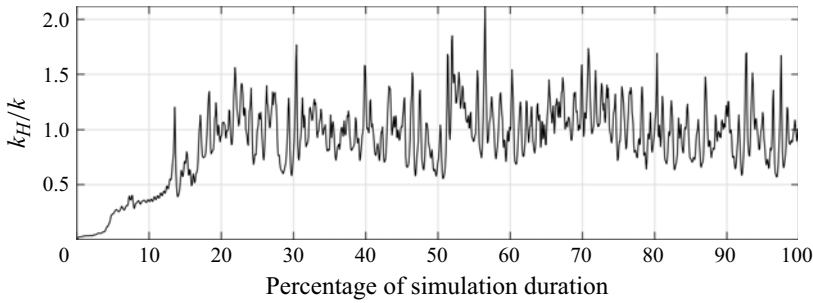


Figure 12. Time series of the volume-averaged horizontal turbulent kinetic energy (k_H) normalised by the volume- and time-averaged turbulent kinetic energy (k) of the V1 simulation as a function of percentage of the total simulation duration (see also [table 1](#)).

Environmental Institute at Princeton University. E.B.Z. is supported by the National Oceanic and Atmospheric Administration, U.S. Department of Commerce by award NA18OAR4320123 (The Cooperative Institute for Modeling the Earth System at Princeton University).

Declaration of interests. The authors report no conflict of interest.

Appendix A. Energy growth of shear modes and statistical convergence

The kinetic energy associated with simulations of triply periodic, forced, strongly stratified turbulence has been observed to accumulate in large-scale horizontal motions referred to as ‘shear modes’ (see earlier discussion by Smith & Waleffe 2002 and more recently by Maffioli 2017; Maffioli, Delache & Godeferd 2020). The energy of these shear modes can grow over long times even after energy in the remaining modes has begun to exhibit statistical stationarity (e.g. figures 6a and 6c of Maffioli *et al.* 2020); so in previous studies, these modes have often been removed to allow for time averaging of the flow statistics. In our simulations, the combination of time-varying forcing and long integration times allow for these shear modes (as well as the remaining modes) to reach statistical stationarity. We demonstrate this in [figure 12](#), which shows the time series of the volume-averaged horizontal kinetic energy (k_H) normalised by the volume- and time-averaged turbulent kinetic energy (k) of the V1 simulation (most stable simulation). We note that k_H/k continues to grow for the first 20 % of the simulation duration, but it begins to fluctuate about its mean value for the latter 80 % of the simulation duration. The remaining V-series simulations have weaker stability, so their k_H values reach statistical stationarity quicker. The role of shear modes could be explored further by applying a decomposition of the flow fields (e.g. $f(\mathbf{x}, t) = \bar{f}(z, t) + f'(\mathbf{x}, t)$, where $\bar{f}(z, t)$ represents the shear modes) and revisiting the energy exchange and flux generation of strongly stratified turbulence (e.g. (3.4)–(3.8)).

Appendix B. Joint p.d.f. and covariance integrand contour plots of pressure correlations

Here, we consider the joint p.d.f.s of the pressure–strain correlations ($p\partial_z w$) in [figure 13](#). There are nine panels, corresponding to the same three stability conditions as in [figure 7](#) (different columns) and three different sets of pressure–strain correlations (total, nonlinear and buoyancy) corresponding to the top, middle and bottom rows. The variables are normalised by the r.m.s. values of the total pressure p and the vertical gradient of the vertical velocity $\partial_z w$. The buoyancy pressure component has a smaller magnitude than

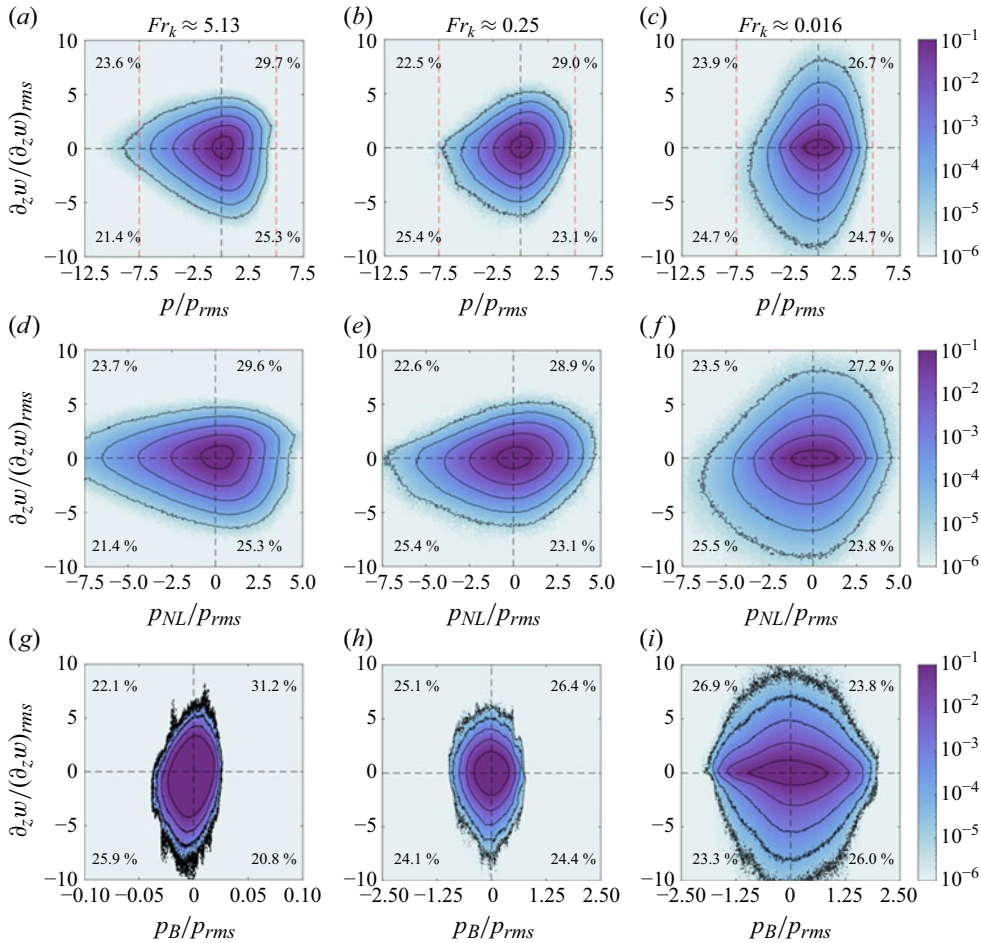


Figure 13. Joint probability distributions for the (a,b,c) total, (d,e,f) nonlinear and (g,h,i) buoyancy pressure–strain correlations normalised by the r.m.s. values of the total pressure p and the vertical gradient of the vertical velocity $\partial_z w$. The three columns correspond to (a,d,g) very weak, (b,e,h) strong and (c,f,i) very strong stability (right). The text in the four corners indicates the probability mass contained within each quadrant.

the nonlinear component (see figure 6a), so the plots in the middle and bottom rows for the nonlinear and buoyancy pressure–strain correlation have modified x -axis limits. When stability is weak, there is largely a compensation between events in quadrants 1, 4 and quadrants 2, 3 for the total pressure–strain correlation (panel a), resulting in the overall pressure–strain correlations being negligible (see also figure 5). As stability increases (panels b,c), however, we observe that the p.d.f. contours shift such that the two variables become more strongly positively correlated. The buoyancy component of the pressure–strain correlations (panels g,h,i) has more events in quadrants 1 and 3 for the weakest stability (panel g), but the p.d.f. contours become more similar across the four quadrants as stability increases (panels h and i) for the four quadrants, albeit with more mass in quadrants 2 and 4, which agrees with the earlier observation that this term on average converts k_w into k_H for $Fr_k < 0.3$ (see figure 6b).

Relatedly, we now plot the covariance integrands associated with these nine joint p.d.f.s in figure 14. The panels are arranged in the same way as in figure 13 with the three stability conditions corresponding to the different columns and the different

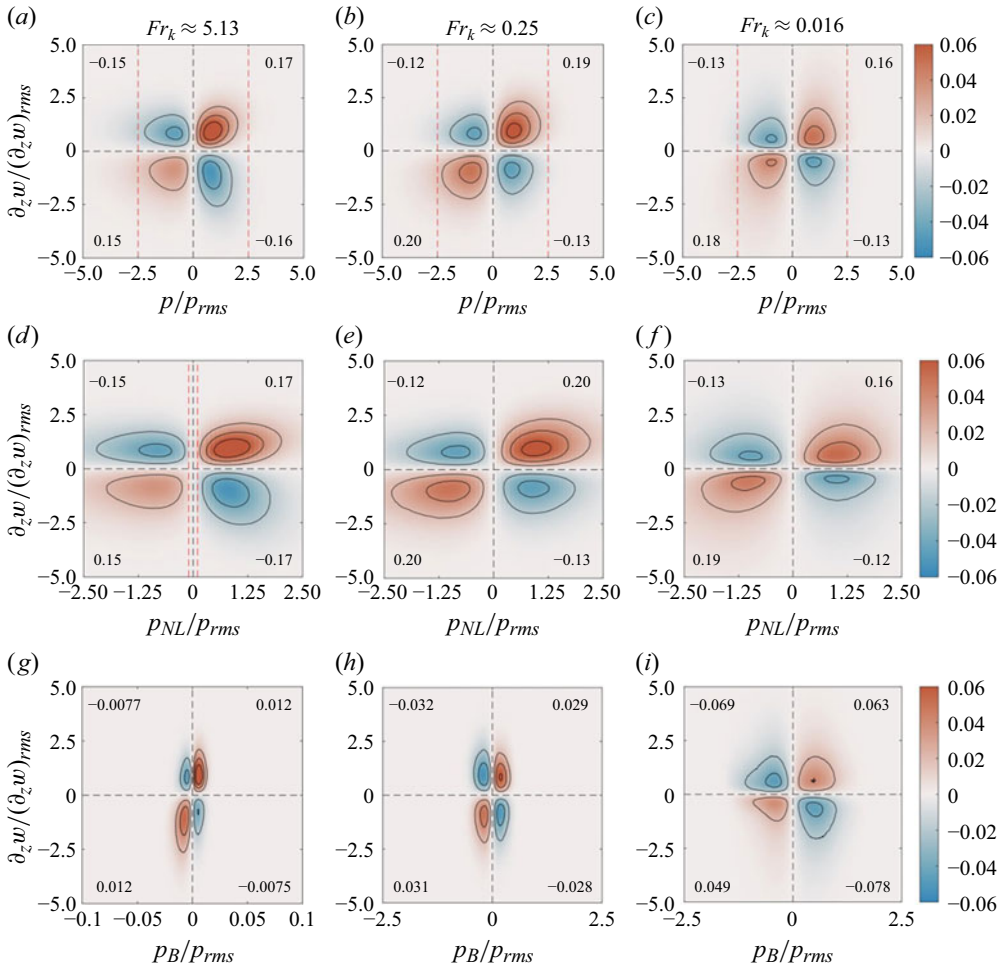


Figure 14. Covariance integrands for the (a,b,c) total, (d,e,f) nonlinear and (g,h,i) buoyancy pressure–strain correlations normalised by the r.m.s. values of the total pressure p and the vertical gradient of the vertical velocity $\partial_z w$. The three columns correspond to (a,d,g) very weak, (b,e,h) strong and (c,f,i) very strong stability. The text in the four corners indicates that quadrant’s contribution to the overall correlation.

sets of pressure–strain correlations corresponding to the different rows. Redistribution from k_H into k_w is shown in red (promotes large-scale isotropy), whereas redistribution from k_w into k_H is shown in blue (promotes large-scale anisotropy). We note for weak stratification that the overall correlation is negligible with contributions from quadrants 1, 4 and quadrants 2, 3 compensating for one another (panel a). While the buoyancy component of the pressure–strain correlations is positively correlated (panel g), it is approximately an order of magnitude smaller than the nonlinear component (panel d). For the strong stability simulation (panels b,e,h), the overall pressure–strain correlations exhibit a stronger correlation (panel b), but the buoyancy component largely cancels out. For the strongest stability simulation (panels c,f,i), the overall correlation is weaker, driven by both a weaker positive correlation of the nonlinear component and a stronger negative correlation of the buoyancy component.

Next, we consider the joint p.d.f.s of the pressure scrambling terms ($p\partial_z\rho$) in figure 15. There are nine panels, corresponding to the same three stability conditions as in figures 7

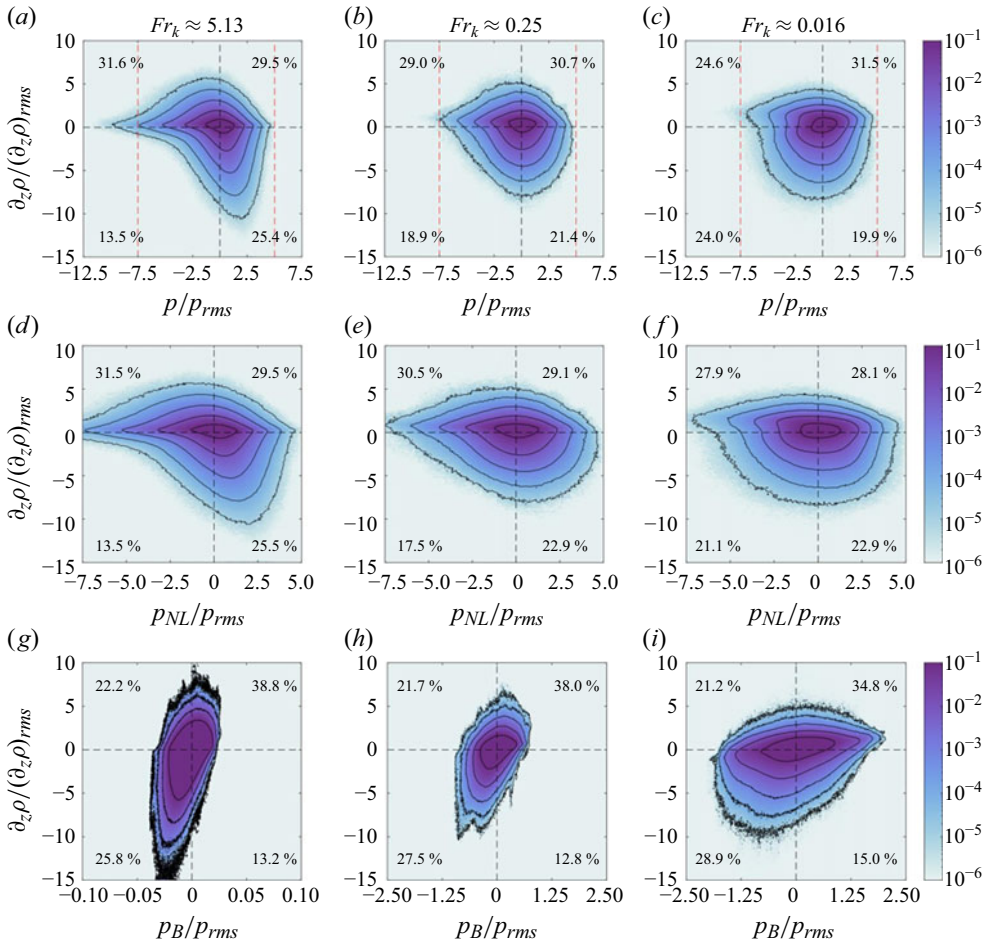


Figure 15. Joint probability distributions for the (a,b,c) total, (d,e,f) nonlinear and (g,h,i) buoyancy pressure scrambling terms normalised by the r.m.s. values of the total pressure p and the vertical gradient of density $\partial_z \rho$. The three columns correspond to (a,d,g) very weak, (b,e,h) strong and (c,f,i) very strong stability. The text in the four corners indicates the probability mass contained within each quadrant.

and 13 (different columns) and three different sets of pressure–strain correlations (total, nonlinear and buoyancy) corresponding to the top, middle and bottom rows. The variables are normalised by the r.m.s. values of the total pressure p and the vertical gradient of the vertical velocity $\partial_z \rho$. As before, because the buoyancy pressure component has a smaller magnitude than the nonlinear component (figure 6a), the plots in the middle and bottom rows for the nonlinear and buoyancy pressure scrambling terms have modified x -axis limits. When stability is weak, the p.d.f. contours of the total pressure scrambling terms are negatively correlated (panel a), but this correlation weakens for strong stability (panel b) and becomes positive for the strongest stability (panel c). The nonlinear component of the pressure scrambling term always has larger probability mass associated with Q2 and Q4 events (middle row), which destroy buoyancy flux, though this weakens with increasing stability. The buoyancy component of the pressure scrambling term is always positively correlated with larger probability masses associated with Q1 and Q3 events (bottom row), which generate vertical buoyancy flux.

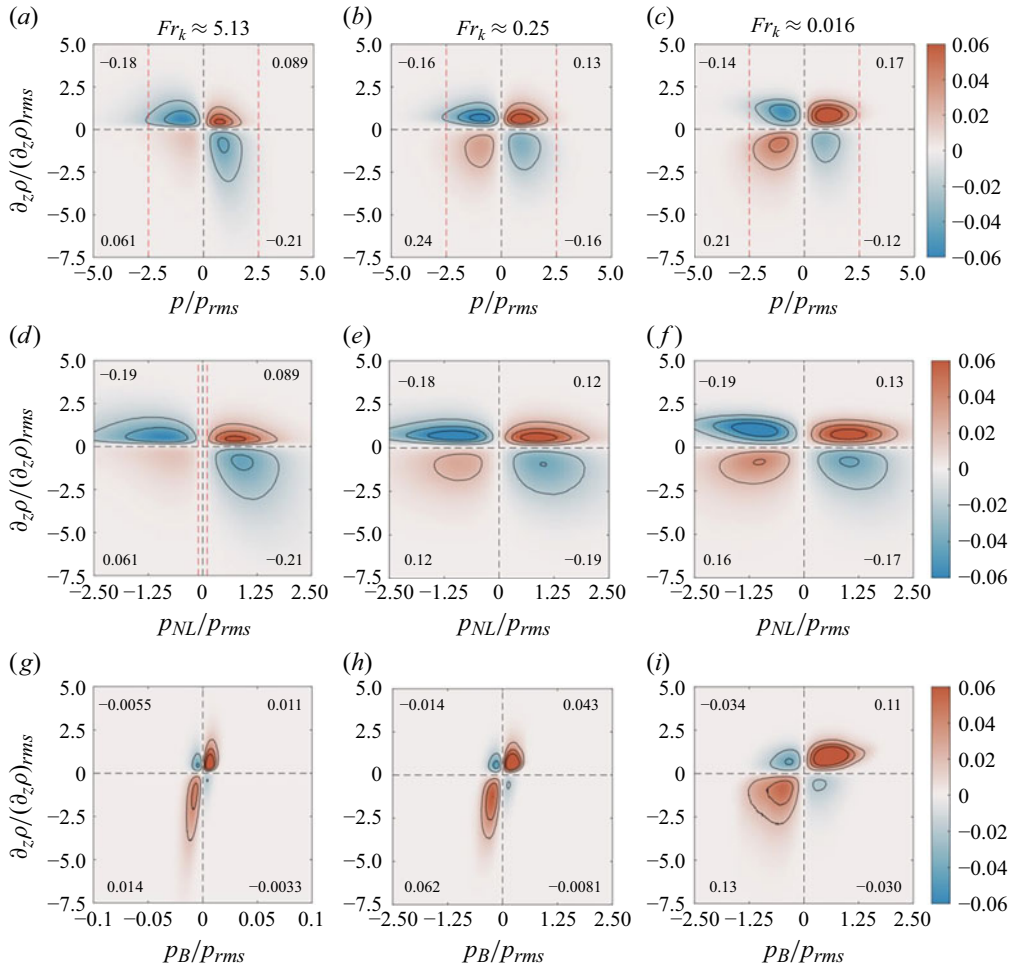


Figure 16. Covariance integrands for the (a,b,c) total, (d,e,f) nonlinear and (g,h,i) buoyancy pressure scrambling term normalised by the r.m.s. values of the total pressure p and the vertical gradient of density $\partial_z \rho$. The three columns correspond to (a,d,g) very weak, (b,e,h) strong and (c,f,i) very strong stability. The text in the four corners indicates that quadrant's contribution to the overall correlation.

We next consider the associated covariance integrands in figure 16 with the same panel arrangements as before. Pressure scrambling correlations that generate buoyancy flux are shown in red, while those that destroy buoyancy flux are shown in blue. For weak stratification, the overall correlation is negative (panel a), and this is due to the nonlinear component (panel d) being more significant than the positively correlated buoyancy component (panel g). For strong stability (panels b,e,h), we note that the overall correlation is near zero, where the nonlinear and buoyancy components largely cancel out. For the strongest stability (panels c,f,i), the buoyancy component is more significant than the nonlinear component, resulting in an overall positive correlation of the total pressure scrambling term (summing up the four numbers in panel c).

REFERENCES

ADCROFT, A., 2019 The GFDL global ocean and sea ice model OM4.0: model description and simulation features. *J. Adv. Model. Earth Syst.* **11** (10), 3167–3211.

- ALLOUCHE, M., BOU-ZEID, E., ANSORGE, C., KATUL, G.G., CHAMECKI, M., ACEVEDO, O., THANEKAR, S. & FUENTES, J.D. 2022 The detection, genesis, and modeling of turbulence intermittency in the stable atmospheric surface layer. *J. Atmos. Sci.* **79**, 1171–1190.
- ALMALKIE, S. & DE BRUYN KOPS, S.M. 2012 Kinetic energy dynamics in forced, homogeneous, and axisymmetric stably stratified turbulence. *J. Turbul.* **13**, N29.
- AUDOUIN, O., ROEHRIG, R., COUVREUX, F. & WILLIAMSON, D. 2021 Modeling the GABLS4 strongly-stable boundary layer with a GCM turbulence parameterization: parametric sensitivity or intrinsic limits? *J. Adv. Model. Earth Syst.* **13** (3), e2020MS002269.
- AYET, A., KATUL, G.G., BRAGG, A.D. & REDELSPERGER, J.L. 2020 Scalewise return to Isotropy in stratified boundary layer flows. *J. Geophys. Res.: Atmos.* **125** (16), e2020JD032732.
- BASAK, S. & SARKAR, S. 2006 Dynamics of a stratified shear layer with horizontal shear. *J. Fluid Mech.* **568**, 19–54.
- BASSENNE, M., URZAY, J., PARK, G.I. & MOIN, P. 2016 Constant-energetics physical-space forcing methods for improved convergence to homogeneous-isotropic turbulence with application to particle-laden flows. *Phys. Fluids* **28** (3), 035114.
- BILLANT, P. & CHOMAZ, J.-M. 2001 Self-similarity of strongly stratified inviscid flows. *Phys. Fluids* **13** (6), 1645–1651.
- BINTANJA, R., VAN DER LINDEN, E.C. & HAZELEGER, W. 2012 Boundary layer stability and Arctic climate change: a feedback study using EC-Earth. *Clim. Dyn.* **39** (11), 2659–2673.
- BOU-ZEID, E., GAO, X., ANSORGE, C. & KATUL, G.G. 2018 On the role of return to isotropy in wall-bounded turbulent flows with buoyancy. *J. Fluid Mech.* **856**, 61–78.
- BRAGG, A.D. & DE BRUYN KOPS, S.M. 2024a Asymptotic analysis of mixing in stratified turbulent flows, and the conditions for an inertial sub-range. [arXiv:2402.10704](https://arxiv.org/abs/2402.10704)
- BRAGG, A.D. & DE BRUYN KOPS, S.M. 2024b Understanding the effect of Prandtl number on momentum and scalar mixing rates in neutral and stably stratified flows using gradient field dynamics. *J. Fluid Mech.* **992**, A10.
- BRYAN, F. 1987 Parameter sensitivity of primitive equation ocean general circulation models. *J. Phys. Oceanogr.* **17** (7), 970–985.
- CAULFIELD, C.P. 2020 Open questions in turbulent stratified mixing: do we even know what we do not know? *Phys. Rev. Fluids* **5** (11), 110518.
- CAULFIELD, C.P. 2021 Layering, instabilities, and mixing in turbulent stratified flows. *Annu. Rev. Fluid Mech.* **53** (1), 113–145.
- CHAMECKI, M., DIAS, N.L. & FREIRE, L.S. 2018 A TKE-based framework for studying disturbed atmospheric surface layer flows and application to vertical velocity variance over canopies. *Geophys. Res. Lett.* **45** (13), 6734–6740.
- CIMOLI, L., CAULFIELD, C.P., JOHNSON, H.L., MARSHALL, D.P., MASHAYEK, A., NAVEIRA GARABATO, A.C. & VIC, C. 2019 Sensitivity of deep ocean mixing to local internal tide breaking and mixing efficiency. *Geophys. Res. Lett.* **46** (24), 14622–14633.
- DALAUDIER, F. & SIDI, C. 1990 Some characteristics of the turbulent buoyancy subrange. *Adv. Space Res.* **10** (10), 37–40.
- DE BRUYN KOPS, S.M. & RILEY, J.J. 2019 The effects of stable stratification on the decay of initially isotropic homogeneous turbulence. *J. Fluid Mech.* **860**, 787–821.
- DE LAVERGNE, C., MADEC, G., LE SOMMER, J., NURSER, A.J.G. & NAVEIRA GARABATO, A.C. 2016 The impact of a variable mixing efficiency on the abyssal overturning. *J. Phys. Oceanogr.* **46** (2), 663–681.
- FOGARTY, J. & BOU-ZEID, E. 2023 The atmospheric boundary layer above the marginal ice zone: scaling, surface fluxes, and secondary circulations. *Boundary-Layer Meteorol.* **189** (1–3), 1–24.
- FOX-KEMPER, B., 2019 Challenges and prospects in ocean circulation models. *Front. Mar. Sci.* **6**.
- FREIRE, L.S., CHAMECKI, M., BOU-ZEID, E. & DIAS, N.L. 2019 Critical flux Richardson number for Kolmogorov turbulence enabled by TKE transport. *Q. J. R. Meteorol. Soc.* **145** (721), 1551–1558.
- GARANAİK, A. & VENAYAGAMOORTHY, S.K. 2019 On the inference of the state of turbulence and mixing efficiency in stably stratified flows. *J. Fluid Mech.* **867**, 323–333.
- GAYEN, B. & SARKAR, S. 2011 Boundary mixing by density overturns in an internal tidal beam. *Geophys. Res. Lett.* **38** (14).
- GERZ, T. & SCHUMANN, U. 1996 A possible explanation of countergradient fluxes in homogeneous turbulence. *Theoret. Comput. Fluid Dyn.* **8** (3), 169–181.
- GNANADESIKAN, A. 1999 A global model of silicon cycling: sensitivity to eddy parameterization and dissolution. *Global Biogeochem. Cycles* **13** (1), 199–220.
- GREGG, M.C., D’ASARO, E.A., RILEY, J.J. & KUNZE, E. 2018 Mixing efficiency in the ocean. *Annu. Rev. Mar. Sci.* **10** (1), 443–473.

- HANJALIĆ, K. & LAUNDER, B.E. 2022 *Modelling Turbulence in Engineering and the Environment: Rational Alternative Routes to Closure*. Cambridge University Press.
- HAO, Z. & GORLÉ, C. 2020 Pressure scrambling effects and the quantification of turbulent scalar flux model uncertainties. *Phys. Rev. Fluids* **5** (8), 082501.
- HEBERT, D.A. & DE BRUYN KOPS, S.M. 2006 Predicting turbulence in flows with strong stable stratification. *Phys. Fluids* **18** (6), 066602.
- HEINZE, R., MIRONOV, D. & RAASCH, S. 2016 Analysis of pressure-strain and pressure gradient-scalar covariances in cloud-topped boundary layers: a large-eddy simulation study. *J. Adv. Model. Earth Syst.* **8** (1), 3–30.
- HENSON, S.A., LAUFKÖTTER, C., LEUNG, S., GIERING, S.L.C., PALEVSKY, H.I. & CAVAN, E.L. 2022 Uncertain response of ocean biological carbon export in a changing world. *Nat. Geosci.* **15** (4), 248–254.
- HOLT, S.E., KOSEFF, J.R. & FERZIGER, J.H. 1992 A numerical study of the evolution and structure of homogeneous stably stratified sheared turbulence. *J. Fluid Mech.* **237**, 499–539.
- HOPFINGER, E.J. 1987 Turbulence in stratified fluids: a review. *J. Geophys. Res.: Oceans* **92** (C5), 5287–5303.
- HOWLAND, C.J., TAYLOR, J.R. & CAULFIELD, C.P. 2020 Mixing in forced stratified turbulence and its dependence on large-scale forcing. *J. Fluid Mech.* **898**.
- ISSAEV, V., WILLIAMSON, N., ARMFELD, S.W. & NORRIS, S.E. 2022 Parameterization of mixing in stratified open channel flow. *J. Fluid Mech.* **935**.
- IVEY, G.N. & IMBERGER, J. 1991 On the nature of turbulence in a stratified fluid. Part I: The Energetics of Mixing. *J. Phys. Oceanogr.* **21** (5), 650–658.
- IVEY, G.N., WINTERS, K.B. & KOSEFF, J.R. 2008 Density stratification, turbulence, but how much mixing? *Annu. Rev. Fluid Mech.* **40** (1), 169–184.
- JAYNE, S.R. 2009 The impact of abyssal mixing parameterizations in an ocean general circulation model. *J. Phys. Oceanogr.* **39** (7), 1756–1775.
- JOHNSON, P.L. 2020 Energy transfer from large to small scales in turbulence by multiscale nonlinear strain and vorticity interactions. *Phys. Rev. Lett.* **124** (10), 104501.
- JOHNSON, P.L. 2021 On the role of vorticity stretching and strain self-amplification in the turbulence energy cascade. *J. Fluid Mech.* **922**.
- KALTENBACH, H.-J., GERZ, T. & SCHUMANN, U. 1994 Large-eddy simulation of homogeneous turbulence and diffusion in stably stratified shear flow. *J. Fluid Mech.* **280**, 1–40.
- KATUL, G.G., PORPORATO, A., SHAH, S. & BOU-ZEID, E. 2014 Two phenomenological constants explain similarity laws in stably stratified turbulence. *Phys. Rev. E* **89** (2), 023007.
- KIMURA, Y. & SULLIVAN, P.P. 2024 2D and 3D properties of stably stratified turbulence. *Atmos.-BASEL* **15** (1), 82.
- LEGASPI, J.D. & WAITE, M.L. 2020 Prandtl number dependence of stratified turbulence. *J. Fluid Mech.* **903**.
- LÉVY, M., COUESPEL, D., HAËCK, C., KEERTHI, M.G., MANGOLTE, I. & PREND, C.J. 2024 The impact of fine-scale currents on biogeochemical cycles in a Changing ocean. *Annu. Rev. Mar. Sci.* **16** (1), 191–215.
- LÉVY, M., FRANKS, P.J.S. & SMITH, K.S. 2018 The role of submesoscale currents in structuring marine ecosystems. *Nat. Commun.* **9** (1), 4758.
- LÉVY, M., KLEIN, P. & TREGUIER, A.M. 2001 Impact of sub-mesoscale physics on production and subduction of phytoplankton in an oligotrophic regime. *J. Mar. Sci.* **59** (4), 535–565.
- LEWIN, S.F. & CAULFIELD, C.P. 2022 Stratified turbulent mixing in oscillating shear flows. *J. Fluid Mech.* **944**.
- LI, D. & BOU-ZEID, E. 2011 Coherent structures and the dissimilarity of turbulent transport of momentum and scalars in the unstable atmospheric surface layer. *Boundary-Layer Meteorol.* **140** (2), 243–262.
- LIN, J.T. & PAO, Y.H. 1979 Wakes in stratified fluids. *Annu. Rev. Fluid Mech.* **11** (1), 317–338.
- LINDBORG, E. 2006 The energy cascade in a strongly stratified fluid. *J. Fluid Mech.* **550**, 207–242.
- LUNDGREN, T.S. 2003 Linearly forced isotropic turbulence. In *Annual Research Briefs*, pp. 461–473. Center for Turbulence Research.
- MAFFIOLI, A. 2017 Vertical spectra of stratified turbulence at large horizontal scales. *Phys. Rev. Fluids* **2** (10), 104802.
- MAFFIOLI, A., BRETHOUWER, G. & LINDBORG, E. 2016 Mixing efficiency in stratified turbulence. *J. Fluid Mech.* **794**.
- MAFFIOLI, A., DELACHE, A. & GODEFERD, F.S. 2020 Signature and energetics of internal gravity waves in stratified turbulence. *Phys. Rev. Fluids* **5** (11), 114802.
- MASHAYEK, A., SALEHIPOUR, H., BOUFFARD, D., CAULFIELD, C.P., FERRARI, R., NIKURASHIN, M., PELTIER, W.R. & SMYTH, W.D. 2017 Efficiency of turbulent mixing in the abyssal ocean circulation. *Geophys. Res. Lett.* **44** (12), 6296–6306.

- MATER, B.D. & VENAYAGAMOORTHY, S.K. 2014a The quest for an unambiguous parameterization of mixing efficiency in stably stratified geophysical flows. *Geophys. Res. Lett.* **41** (13), 4646–4653.
- MATER, B.D. & VENAYAGAMOORTHY, S.K. 2014b A unifying framework for parameterizing stably stratified shear-flow turbulence. *Phys. Fluids* **26** (3), 036601.
- MONISMITH, S.G., KOSEFF, J.R. & WHITE, B.L. 2018 Mixing efficiency in the presence of stratification: when is it constant? *Geophys. Res. Lett.* **45** (11), 5627–5634.
- NGUYEN-DANG, C., WILLIAMSON, N., ARMPFIELD, S.W., KIRKPATRICK, M.P. & NORRIS, S.E. 2023 *Stratification and Temporal Evolution of Mixing Regimes in Diurnally Heated River Flows*. *Environ Fluid Mech.*
- ONUKI, Y., JOUBAUD, S. & DAUXOIS, T. 2021 Simulating turbulent mixing caused by local instability of internal gravity waves. *J. Fluid Mech.* **915**.
- OSBORN, T.R. 1980 Estimates of the local rate of vertical diffusion from dissipation measurements. *J. Phys. Oceanogr.* **10** (1), 83–89.
- PEARSON, B.C., GRANT, A.L.M. & POLTON, J.A. 2019 Pressure–strain terms in Langmuir turbulence. *J. Fluid Mech.* **880**, 5–31.
- PETROPOULOS, N., COUCHMAN, M.M.P., MASHAYEK, A., DE BRUYN KOPS, S.M. & CAULFIELD, C.P. 2024 Prandtl number effects on extreme mixing events in forced stratified turbulence. *J. Fluid Mech.* **983**, R1.
- POLZIN, K.L. 2009 An abyssal recipe. *Ocean Model.* **30** (4), 298–309.
- POPE, S.B. 2000 *Turbulent Flows*. Cambridge University Press.
- PORTÉ-AGEL, F., BASTANKHAH, M. & SHAMSODDIN, S. 2020 Wind-turbine and wind-farm flows: a review. *Boundary-Layer Meteorol.* **174** (1), 1–59.
- PORTWOOD, G.D., DE BRUYN KOPS, S.M. & CAULFIELD, C.P. 2019 Asymptotic dynamics of high dynamic range stratified turbulence. *Phys. Rev. Lett.* **122** (19), 194504.
- RAHMANI, M., SEYMOUR, B.R. & LAWRENCE, G.A. 2016 The effect of Prandtl number on mixing in low Reynolds number Kelvin–Helmholtz billows. *Phys. Fluids* **28** (5), 054107.
- RESPLANDY, L., LÉVY, M. & MCGILLICUDDY, JR., D.J. 2019 Effects of eddy-driven subduction on ocean biological carbon pump. *Global Biogeochem. Cycles* **33** (8), 1071–1084.
- RILEY, J.J., COUCHMAN, M.M.P. & DE BRUYN KOPS, S.M. 2023 The effect of Prandtl number on decaying stratified turbulence. *J. Turbul.* **0** (0), 1–19.
- RILEY, J.J. & DE BRUYN KOPS, S.M. 2003 Dynamics of turbulence strongly influenced by buoyancy. *Phys. Fluids* **15** (7), 2047–2059.
- RILEY, J.J. & LELONG, M.-P. 2000 Fluid motions in the presence of strong stable stratification. *Annu. Rev. Fluid Mech.* **32** (1), 613–657.
- ROSALES, C. & MENEVEAU, C. 2005 Linear forcing in numerical simulations of isotropic turbulence: physical space implementations and convergence properties. *Phys. Fluids* **17** (9), 095106.
- ROTTA, J. 1951 Statistische theorie nichthomogener turbulenz. *Z. Physik* **129** (6), 547–572.
- SALEHIPOUR, H. & PELTIER, W.R. 2015 Diapycnal diffusivity, turbulent Prandtl number and mixing efficiency in Boussinesq stratified turbulence. *J. Fluid Mech.* **775**, 464–500.
- SALEHIPOUR, H., PELTIER, W.R. & MASHAYEK, A. 2015 Turbulent diapycnal mixing in stratified shear flows: the influence of Prandtl number on mixing efficiency and transition at high Reynolds number. *J. Fluid Mech.* **773**, 178–223.
- SHAH, S.K. & BOU-ZEID, E. 2014 Direct numerical simulations of turbulent Ekman layers with increasing static stability: modifications to the bulk structure and second-order statistics. *J. Fluid Mech.* **760**, 494–539.
- SHIH, L.H., KOSEFF, J.R., IVEY, G.N. & FERZIGER, J.H. 2005 Parameterization of turbulent fluxes and scales using homogeneous sheared stably stratified turbulence simulations. *J. Fluid Mech.* **525**, 193–214.
- SMITH, L.M. & WALEFFE, F. 2002 Generation of slow large scales in forced rotating stratified turbulence. *J. Fluid Mech.* **451**, 145–168.
- ST. LAURENT, L.C., SIMMONS, H.L. & JAYNE, S.R. 2002 Estimating tidally driven mixing in the deep ocean. *Geophys. Res. Lett.* **29** (23), 21–1–21–4.
- STEVENS, R.J.A.M. & MENEVEAU, C. 2017 Flow structure and turbulence in wind farms. *Annu. Rev. Fluid Mech.* **49**, 311–339.
- TAYLOR, J.R. & THOMPSON, A.F. 2023 Submesoscale dynamics in the Upper ocean. *Annu. Rev. Fluid Mech.* **55** (1), 103–127.
- TU, J., FAN, D., LIU, Z. & SMYTH, W. 2022 Scaling the mixing efficiency of sediment-stratified turbulence. *Geophys. Res. Lett.* **49** (13), e2022GL099025.
- VENAYAGAMOORTHY, S.K. & KOSEFF, J.R. 2016 On the flux Richardson number in stably stratified turbulence. *J. Fluid Mech.* **798**.

- VLAYKOV, D.G. & WILCZEK, M. 2019 On the small-scale structure of turbulence and its impact on the pressure field. *J. Fluid Mech.* **861**, 422–446.
- WAITE, M.L. & BARTELLO, P. 2004 Stratified turbulence dominated by vortical motion. *J. Fluid Mech.* **517**, 281–308.
- WALLACE, J.M. 2016 Quadrant analysis in turbulence research: history and evolution. *Annu. Rev. Fluid Mech.* **48** (2016), 131–158.
- WILLIAMSON, N., ARMFIELD, S.W., KIRKPATRICK, M.P. & NORRIS, S.E. 2015 Transition to stably stratified states in open channel flow with radiative surface heating. *J. Fluid Mech.* **766**, 528–555.
- WILLIAMSON, N., ARMFIELD, S.W. & LIN, W. 2011 Forced turbulent fountain flow behaviour. *J. Fluid Mech.* **671**, 535–558.
- WUNSCH, C. & FERRARI, R. 2004 Vertical mixing, energy, and the general circulation of the oceans. *Annu. Rev. Fluid Mech.* **36** (1), 281–314.
- YI, Y.R. & KOSEFF, J.R. 2022a Dynamics and energetics underlying mixing efficiency in homogeneous stably stratified turbulence. *Phys. Rev. Fluids* **7** (8), 084801.
- YI, Y.R. & KOSEFF, J.R. 2022b Revised mixing coefficient scaling for sheared stably stratified turbulence. *J. Fluid Mech.* **952**, A18.
- YI, Y.R. & KOSEFF, J.R. 2023 Underlying physics of mixing efficiency for shear-forced, stratified turbulence. *Phys. Rev. Fluids* **8**(8), 084803.
- ZHANG, X., DHARIWAL, R., PORTWOOD, G., DE BRUYN KOPS, S.M. & BRAGG, A.D. 2022 Analysis of scale-dependent kinetic and potential energy in sheared, stably stratified turbulence. *J. Fluid Mech.* **946**.